AN ANALYSIS OF ELECTROHYDRODYNAMIC STABILITY AND DEFORMATION IN IMMISCIBLE FLUIDS

BY JIA ZHANG

A dissertation submitted to the

Graduate School—New Brunswick

Rutgers, The State University of New Jersey

in partial fulfillment of the requirements

for the degree of

Doctor of Philosophy

Graduate Program in Mechanical and Aerospace Engineering

Written under the direction of

Professor Hao Lin

and approved by

New Brunswick, New Jersey

October, 2012

ABSTRACT OF THE DISSERTATION

An Analysis of Electrohydrodynamic Stability and Deformation in Immiscible Fluids

by Jia Zhang

Dissertation Director: Professor Hao Lin

The interactions between an electric field and fluid motion give rise to a class of complex and important phenomena known as electrohydrodynamics. In this work, we developed a set of analytical tools to provide basic understanding and quantitative prediction capabilities. Under this theme, three tasks have been accomplished. 1. A general solution approach for the electrohydrodynamic instability of stratified immiscible fluids is presented. The problems of two and three fluid layers subject to normal electric fields are analyzed. Analytical solutions are obtained by employing the transfer relations relating the disturbance stresses to the flow variables at the interface(s). The results assume a general format. Both new dispersion relations and those from various previous work are shown to be special cases when proper simplifications are considered. As a specific example, the stability behavior of a three-layer channel flow is investigated in details using this framework. This work provides a unifying method to treat a generic class of instability problems. 2. A transient analysis to quantify droplet deformation under DC electric fields is presented. The full Taylor-Melcher leaky dielectric model is employed where the charge relaxation time is considered to be finite. The droplet is assumed to be spheroidal in shape for all times. The main result is an ODE governing the evolution of the droplet aspect ratio. The model is validated by extensively comparing predicted deformation with both previous theoretical and numerical studies, and with experimental data. Furthermore, the effects of parameters and stresses on deformation characteristics are systematically analyzed taking advantage of the explicit formulae on their contributions. The theoretical framework lays the foundation for the study of a more complex problem, vesicle electrodeformation. 3. A transient analysis for vesicle deformation under DC electric fields is developed. The theory extends from a droplet model, with the additional consideration of a lipid membrane separating two fluids of arbitrary properties. For the latter, both a membrane-charging and a membrane-mechanical model are supplied. The main result is also an ODE governing the evolution of the vesicle aspect ratio. The effects of initial membrane tension and pulse length are examined. The model prediction is extensively compared with experimental data, and is shown to accurately capture the system behavior in the regime of no or weak electroporation. More importantly, the comparison reveals that vesicle relaxation obeys a universal behavior regardless of the means of deformation. The process is governed by a single timescale that is a function of the vesicle initial radius, the fluid viscosity, and the initial membrane tension. This universal scaling law can be used to calculate membrane properties from experimental data. Together, these projects provide powerful tools to analyze a broad class of problems involving electrostatics, hydrodynamics, and membrane mechanics.

Acknowledgements

First and foremost, I would like to express my sincere gratitude to my advisor, Professor Hao Lin. This dissertation is accomplished with his inspiration and guidance. In the past five years, Dr. Lin has been a mentor whose critical thinking, rigorous attitude, and encouragement thrust me forward. He has not only taught me how to conduct independent research, but also provided me with many advices on my life. It is a great pleasure to work with him.

I am grateful to my collaborator, Professor Jeffrey D. Zahn at Rutgers University for providing insightful comments; Professor Yuan-Nan Young at New Jersey Institute of Technology for validating my mathematical derivation. I would like to express my gratitude to my committee members, Professor Tobias Rossmann and Professor Doyle Knight at Rutgers University for providing valuable suggestions.

I would also like to thank my colleague Jianbo Li for his help in developing droplet electrodeformation model; Mohamed Sadik for sharing his experimental data; Miao Yu for his advices on constructing a membrane-charging model. My special thanks to all my friends for their sincere friendship and support in the past years.

Finally, I would like to express my deepest gratitude to my parents, Muliang Zhang and Yan Chen for their unconditional love and support.

Table of Contents

Abstract ii

Acknowledgements iv

List of Tables viii

List of Figures ix

1. Introduction 1

- 1.1. Electrohydrodynamic instability 2
- 1.2. Electrohydrodynamic deformation of droplets 4
- 1.3. Electrohydrodynamic deformation of vesicles 6

2. A General Analysis for The Electrohydrodynamic Instability of Stratified Immiscible Fluids 9

- 2.1. Introduction 9
- 2.2. Theory 9
- 2.3. Specific cases 17
  - 2.3.1. Two semi-infinite layers ($a,\ b \to \infty$) 17
  - 2.3.2. Two finite layers 18
  - 2.3.3. Three layers, infinite domain ($a \to \infty$) 20
  - 2.3.4. Three finite layers 21
- 2.4. Instability behavior for a three-layer channel flow 21
  - 2.4.1. The zero-Reynolds-number limit ($Re \to 0$) 21
  - 2.4.2. Finite Reynolds numbers 23
  - 2.4.3. A comparison with experimental data 28
- 2.5. Conclusions 29

3. A Transient Analysis for Droplet Electrodeformations 30

3.1. Introduction 30

3.2. Theory 30

3.2.1. The electrical problem 32

3.2.2. The hydrodynamic problem 35

3.3. Comparison with previous results 38

3.3.1. Comparison with previous theories and simulation 39

3.3.2. Comparison with experimental data 41

3.4. The effects of stresses on deformation 44

3.5. Conclusions 46

4. A Transient Analysis for Vesicle Electrodeformations 48

4.1. Introduction 48

4.2. Theory 49

4.2.1. The electrical problem 49

4.2.2. The hydrodynamic problem 52

4.2.3. The membrane-mechanical model 53

4.2.4. General solution 54

4.2.5. A similarity solution for vesicle relaxation 56

4.3. Results 57

4.3.1. The effects of Γ_0 and t_p 58

4.3.2. Comparison with experimental data 61

4.4. Conclusions 66

5. Conclusions 67

Appendix A. The derivation of the transfer relations 69

Appendix B. Three layers in the limit of a, $\sigma_r \to \infty$ 70

Appendix C. Expressions of $f_{11}(\xi_0) - f_{15}(\xi_0)$, $f_{21}(\xi_0) - f_{24}(\xi_0)$, and F . . . 71

Curriculum Vitae 82

List of Tables

2.1. List of model parameters. The parameters are chosen following Zahn and Reddy [86]. 24

2.2. Comparison of the wavenumber for the fastest-growing mode, k_{max}, from measurements by Zahn and Reddy (2006, denoted "measured"), the current model, and the prediction via a simplified model assuming $\sigma_r \to \infty$ (also from Zahn and Reddy [86], denoted "ZR2006"). 28

4.1. List of parameters for figure 4.5. For each case, E_0 and t_p are specified according to RD05. Γ_0 is a fitting parameter to obtain best comparison between simulation and data. For cases b, d, e, and f, extended pulse lengths (denoted by star) are also used. 60

List of Figures

2.1. Schematics of the two generic problem configurations. 11

2.2. Typical streamline patterns for the (a) kink and (b) sausage mode of the three-layer problem. The dashed lines denote the interfacial positions. A '+' or '−' sign denotes a local maximum or minimum of the stream function, respectively. 17

2.3. Phase diagram for the (a) kink, and (b) sausage mode. Here T denotes a destabilizing tangential stress; and N, a destabilizing normal stress. The shaded areas denote regions of stability where both stresses have stabilizing effects. 23

2.4. The real growth rate as a function of the wavenumber for the (a) kink, and (b) sausage mode. The wavenumber at which the maximum growth rate (s_{max}) occurs is denoted k_{max} (see, e.g. the black dots for E_{app}=4 kV/cm). 24

2.5. Contour plot of the maximum growth rate (s_{max}, in the unit of s^{-1}) for the (a) kink, and (b) sausage mode. Here S denotes a stable region, and U denotes an unstable region. 25

2.6. Contour plot of the maximum wavenumber (k_{max}) for the (a) kink, and (b) sausage mode. 26

2.7. The effect of the applied electric field on the neutral stability curve for the (a) kink, and (b) sausage mode. The stable region shrinks as the field strength increases. 27

2.8. (a) Comparison of the maximum growth rate between the kink and sausage modes for E_{app}=3 kV/cm. A kink dominant region suggests that the kink mode grows more rapidly than the sausage mode. (b) An increasing field strength expands the kink-dominant region at the expense of the sausage-dominant region. 27

3.1. (a) A schematic of the problem configuration. (b) The prolate spheroidal coordinate system. 32

3.2. The equilibrium aspect ratio as a function of electric capillary number. The parameters are $\sigma_r = 1.19\times10^{-2}$, $\epsilon_r = 3.24\times10^{-1}$, and $\mu_r = 7.33\times10^{-2}$. 39

3.3. The deformation of a conducting droplet in a highly viscous medium. (a) $Ca_E = 0.18$ and 0.204. (b) $Ca_E = 0.206$ and 0.21. The dimensionless time τ is defined as $\tau = t/\tau_2$, where $\tau_2 = r_0\mu_e/\gamma$. 40

3.4. The prediction from current model is compared with the small deformation theories [1, 74] and experimental data [24]. The parameters are $\sigma_r = 0.03$, $\epsilon_r = 0.73$, and $\mu_r = 1.14$. 42

3.5. Comparison of transient droplet deformation. (a) A water droplet in silicone oil. The parameters are $\sigma_r = 1 \times 10^{-6}$, $\epsilon_r = 3.55 \times 10^{-2}$, $\mu_r = 1000$, $E_0 = 3.2$ kV/cm, $r_0 = 0.25$ cm, $\mu_e = 0.98$ Pa $\cdot$ s, $\epsilon_e = 2.478 \times 10^{-11}$ F/m, and $\gamma = 3.037 \times 10^{-2}$ N/m. (b) A water-ethanol droplet in silicone oil. The parameters are $\sigma_r = 1 \times 10^{-5}$, $\epsilon_r = 0.05$, $\mu_r = 23.3$, $E_0 = 4.5$ kV/cm, $r_0 = 0.14$ cm, $\mu_e = 0.98$ Pa $\cdot$ s, $\epsilon_e = 2.478\times10^{-11}$ F/m, and $\gamma = 3.432 \times 10^{-2}$ N/m. 43

3.6. Droplet deformation in the limit of extremely low conductivities. The parameters are $\sigma_r = 0.03$, $\epsilon_r = 0.73$, $\mu_r = 1.14$, $E_0 = 3.2$ kV/cm, $r_0 = 0.16$ cm, $\mu_e = 0.9$ Pa $\cdot$ s, $\epsilon_e = 2.478 \times 10^{-11}$ F/m, and $\gamma = 5 \times 10^{-3}$ N/m. The best agreement between the data and the theory is found for $\sigma_e = 7 \times 10^{-12}$ S/m. For reference, the dotted line shows the calculation according to the instantaneous-charge-relaxation (ICR) model. 44

3.7. Phase diagram for droplet deformation. Here the dotted line is calculated by satisfying $Q_T = 0$. The solid line is calculated by solving for the root of Taylor's discriminating function. The dashed line represents $Q_N = 0$. Pr and Ob denote prolate and oblate deformation, respectively. N and T denote the effect of normal and tangential stresses, respectively, and a $'+'$ or $'-'$ sign denotes facilitating or suppressing, respectively. 46

3.8. The behavior of equilibrium droplet deformation in different regimes. For $\sigma_r = 0.05$, $Q_T > 0$; $\sigma_r = 1$, $Q_T = 0$; $\sigma_r = 30$, $Q_T < 0$. As $Ca_E \to \infty$, an equilibrium shape is only possible in the T^- regime. Other parameters are $\epsilon_r = 10$ and $\mu_r = 1$. 47

4.1. A schematic of the problem configuration. The original radius of the vesicle is r_0. The conductivity is denoted by σ, the permittivity is denoted by ϵ, the viscosity is denoted by μ, and the subscripts i and e denote intravesicular and extravesicular, respectively. The strength of the applied electric field is E_0. 49

4.2. The relative increase of the apparent area, Δ, as a function of membrane tension, Γ_h, for different values of initial membrane tension, Γ_0. The inset shows the linear regime for larger Γ_h values. 54

4.3. Vesicle deformation-relaxation as a function of Γ_0. The governing parameters are $\sigma_i = 6 \times 10^{-4}$ S/m, $\sigma_e = 4.5 \times 10^{-4}$ S/m, $E_0 = 1$ kV/cm, $t_p = 250\ \mu$s, and $r_0 = 15\ \mu$m. (a) The transmembrane potential at the cathode-facing pole. (b) The time-course of the aspect ratio. (c) The maximum aspect ratio as a function of Γ_0. (d) The similarity behavior in relaxation. The descending branches from (b) are rescaled with $\tau = t/\tau_2$. The thick solid curve is directly obtained by integrating equation (4.31). 59

4.4. Vesicle deformation-relaxation as a function of t_p. The parameters are the same as in figure 4.3. The initial tension is set to be constant, $\Gamma_0 = 1 \times 10^{-6}$ N/m. (a) The time-course of the aspect ratio. (b) The similarity behavior is observed by shifting the relaxation curves with respect to time. The relaxation timescale, $\tau_2 = r_0\mu_e/\Gamma_0$, is the same for all cases. The thick solid curve is directly obtained by integrating equation (4.31). 60

4.5. Comparison with the deformation-relaxation data from RD05. For all cases, $r_0 = 15\,\mu$m, $\sigma_i = 6 \times 10^{-4}$ S/m, and $\sigma_e = 4.5 \times 10^{-4}$ S/m. Parameters specific to each case are listed in table 4.1. The data is represented by symbols, and the simulation is represented by solid curves. For cases b, d, e, and f, the dashed lines represent the simulated results with extended pulses (denoted by stars in table 4.1). 62

4.6. The similarity behavior of vesicle relaxation. The experimental data from cases a-g in figure 4.5 are shifted in time, then rescaled by $\tau_2 = r_0\mu_e/\Gamma_0$. They are represented by symbols. The solid curves are calculated with equation (4.31). The same data are shown on both a semi-log (a) and a linear (b) scale. The coefficient of determination is $R^2 = 0.96$. 64

4.7. Comparison with data from S11. (a) Simulated time-course of the aspect ratio for various conductivity ratios. For all cases $r_0 = 11.3\ \mu$m and $\Gamma_0 = 1 \times 10^{-8}$ N/m. (b) The aspect ratio at $t = 500\ \mu$s as a function of $1/\sigma_r$. 65

Chapter 1

Introduction

Electrohydrodynamics (EHD) is the study of interactions between electric fields and fluid motion [48, 67]. When an electric field is applied, electrostatic forces are usually generated due to variations in fluid properties. These forces are often strong enough to drive a hydrodynamic flow and lead to complex flow patterns such as instability [5, 11, 27, 28, 39, 41, 42, 43, 46, 47, 56, 57, 61, 71, 76, 79, 78, 86] and interfacial deformation [1, 2, 6, 7, 16, 19, 20, 24, 26, 37, 50, 66, 70, 73, 74, 77, 80]. Extensive EHD research has been conducted due to its relevance in various industrial applications. On the macroscale, EHD can be leveraged to enhance heat and mass transfer [85] and pumping performance [45]. On the microscale, EHD is employed to generate droplets [24], mix fluids [42], help purify DNA [86], and promote cell transfection [40]. In this work, we are more interested in EHD flows with microscale configurations.

The electrostatic forces in EHD flows can be generated in two manners. In the first, the fluid is usually a single electrolyte with concentration gradients. An electrical body force is generated in the bulk, which couples the evolution of both the electric fields and fluid motion. This type of flow is termed bulk-coupled EHD. In the second, two or more immiscible fluids with different properties such as conductivity and permittivity are often involved and the electrostatic forces are absent except at the fluid interfaces. In this case, the hydrodynamic and electrical problems are coupled only through interfacial matching conditions. This type of flow is termed surface-coupled EHD.

In this work, we focus on studying surface-coupled EHD flows. This type of flow is more amenable to theoretical analysis, in contrast to the bulk-coupled problem which usually requires numerical simulations. We have investigated three problems of significance in both fundamental understanding and relevance to applications.

1. We developed a general analysis for the EHD instability of stratified fluids. The main contribution is that we present a unified approach which includes all previous studies as special limiting cases. In addition, using this method we have also generated new dispersion relations not available before, which significantly improve from the previous results when compared with experimental data. This work has been summarized in a publication in Journal of Fluid Mechanics [88].
2. We developed a transient analysis of droplet deformations under electric fields. The analysis is general by assuming arbitrary fluid properties. The results are directly compared with numerical simulations and experimental measurements to reveal good quantitative agreements. Such model is previously not available. Furthermore, the effects of parameters and stresses on deformation characteristics are systematically analyzed taking advantage of the explicit formulae on their contributions. This work has been summarized in a manuscript submitted to Journal of Fluid Mechanics [89].
3. Extending from task two above, we have also constructed an analytical solution for transient, large electrodeformations of vesicles. In this case, we need to incorporate a membrane-charging and a membrane-mechanical model for the lipid membrane in addition. Similarly, the results provide predictions in quantitative agreements with experimental data, and physical insights on membrane behavior and properties. This work has been summarized in a manuscript submitted to Journal of Fluid Mechanics [90]. In what follows, the specific background and motivation for each project is introduced.

1.1 Electrohydrodynamic instability

EHD instability has been an important subject of study due to its relevance in a variety of microfluidic electrokinetic applications [8, 54, 56]. The present work is motivated by the need to develop efficient microfluidic DNA purification devices. In this technique, aqueous buffer with lysed cellular components flows in parallel with an organic liquid (phenol) into a microchannel. Membrane and other components partition into the organic phase, whereas DNA remains in the aqueous phase, achieving a purification effect. To enhance partitioning efficiency, the interfacial area between the two streams needs to be maximized. In a microfluidic platform, this task can be accomplished by breaking one stream (phase) into droplets using EHD instability and has been realized by [86]. The EHD instability can arise in the bulk of a single, miscible fluid, or at the interface of two immiscible fluids. In the first, bulk-coupled EHD instability, an electrical body force appears explicitly in the Navier-Stokes equation [5, 11, 27, 28, 41, 42, 43, 61, 71]. This force drives the instability, and competes with a stabilizing effect due to the diffusive relaxation of the electrical conductivity gradient. In the second, surface-coupled EHD instability, the electrostatic forcing only appears in the interfacial matching conditions [39, 46, 47, 55, 57, 76, 79, 78, 86]. For this case, the conductivity discontinuity across the interface remains a source of the induced stress due to the immiscibility, and the main stabilizing force is the surface tension between the fluids. A comprehensive review summarizing the theoretical foundation, the Taylor-Melcher leaky dielectric model, is given by Saville [67].

This work focuses on a solution method of the second kind, namely, surface-coupled EHD instability. This type of problem is more amenable to theoretical analysis when compared with its bulk-coupled counterpart due to the confinement of the electrostatic forcing to the interfaces. Historically, analytical dispersion relations of the linearized problem have been obtained, largely under two specific situations: 1) $Re \to 0$. Solutions using this (Stokes flow) assumption can be found in, e.g. [12, 76, 78]. 2) An infinite geometry with two- or three-layers of stratified fluid [46, 47, 49, 57]. In addition, some authors also analyzed the stability behavior in the limit of a zero wavenumber (long wave analysis, [39]). In all of the above, a common strategy involves the solution of the electrical and the hydrodynamic problem separately, and the subsequent matching of them at the interfaces. An eigenvalue problem is then formed from which the dispersion relation is sought.

In this work, we present an alternative approach. We employ the ‘transfer relations’ to study the instability of two and three stratified fluid layers. The availability of these relations ensures a straightforward solution without assumptions on the Reynolds number, the geometry, or fluid properties such as conductivity and permittivity. Consequently, the results not only encompasses many disparate ones from the literature, but also engender new ones that are previously not studied. Specifically, we will demonstrate in that we can recover prior results by evaluating our solutions in the proper simplifying limits. More importantly, the dispersion relations for the following new cases are also presented:

(a) A two-layer channel flow with a finite Reynolds number;

(b) A three-layer problem with semi-infinite upper and lower layers, and with an applied field normal to the fluid interfaces;

(c) A three-layer channel flow.

We pursue a more detailed investigation of the last case, namely, the three-layer channel flow. This flow configuration is important for microfluidic mixing and droplet generation applications, and has been experimentally implemented by Zahn and Reddy [86]. We will map the instability behavior in the phase space of the conductivity and permittivity ratios, and with respect to variations in applied field strength. More interestingly, we examine and compare two distinctive instability modes termed the “kink” and “sausage”. This case study demonstrates the utility of our method. This work presents a unifying framework to treat a generic class of surface-coupled EHD instability problem.

1.2 Electrohydrodynamic deformation of droplets

EHD deformation, also known as electrodeformation, of droplets is another class of complex responses of fluids under the influence of an applied electric field. In this case, electrostatic forces are similarly generated at the interface to drive the deformation. Extensive research on this phenomenon has been conducted to study the deformation due to its relevance in a variety of industrial applications, including electrohydrodynamic atomization [84], electrohydrodynamic emulsification [32], and ink-jet printing [4], among others. Historically, the deformation dynamics is divided into two regimes: electrohydrostatics (EHS) and electrohydrodynamics (EHD). In the first, EHS deformation, the droplet is idealized as a perfect conductor immersed in a perfect insulating fluid; or both of the fluids are treated as perfect dielectrics with no free charge [2, 16, 24, 50, 70, 73]. For this case, the electric field only induces a normal electrostatic stress, which is balanced by surface tension, and the final equilibrium shape is always prolate. At the steady state, the hydrodynamic flow is usually absent. In the second, EHD deformation, both fluids are considered to be leaky dielectrics [1, 6, 7, 19, 20, 24, 26, 37, 66, 70, 74, 77, 80]. For this case, when an electric field is applied, free charges accumulate on the droplet surface which induces a tangential electrostatic stress in addition to the normal one. Driven by this force, the fluids inside and outside the droplet present toroidal circulations and a viscous stress is generated in response to balance the tangential electrostatic stress [74]. The droplet deforms into either a prolate or an oblate spheroid shape depending on the specific electrical properties of the fluids. With different electrical properties, the effects of the electrostatic and hydrodynamic stresses on droplet deformation are distinctive.

This work focuses on a solution method for problems of the second kind, namely, EHD deformation. This type of problem is more challenging to solve. In the literature, all theoretical solutions were obtained largely under two specific assumptions: (i) The deformations are small. The analysis is performed by assuming that the equilibrium shape of the droplet only slightly deviates from sphericity. Solutions using this assumption can be found in [1], [74], and [77]. (ii) For large deformations, the shape is assumed to be spheroidal during the entire deformation process. Results using this assumption are given in [7]. When compared with experimental data, predictions from the small-deformation theories always quantitatively underpredict the aspect ratio especially when the deformation is large. In contrast, the large-deformation theory has a better agreement both qualitatively and quantitatively. In all of the above, the theoretical analysis only leads to solutions in the steady state. The Taylor-Melcher leaky dielectric model [48, 67, 88] with the assumption of instantaneous charge relaxation has always been used. On the other hand, the theoretical analysis of transient droplet deformation seems to attract less attention. Only Dubash and Mestel [16] developed a transient deformation theory for an inviscid, conducting droplet. This analysis, which solves a EHS deformation problem, is not applicable to study EHD deformations. In general, to fully solve the transient EHD problem, numerical simulations have been employed [6, 19, 26, 37].

In this work, we present a transient analysis of droplet deformation under direct-current (DC) electric fields. Following Bentenitis and Krause [7], we assume the droplet remains spheroidal in shape. The full Taylor-Melcher leaky dielectric model is employed where the charge relaxation time is considered finite. In this framework, instantaneous charge relaxation is treated as a special limiting case. This generalization allows direct comparison with experimental data which were usually obtained in fluids with very low conductivities ([24]). The main result is an ordinary differential equation (ODE) governing the evolution of the droplet aspect ratio. The availability of this equation allows us to explicitly analyze the effects of parameters and stresses on the deformation characteristics. The model is validated by extensively comparing predicted deformation with both previous theoretical and numerical studies, and with experimental data. The current analysis provides a powerful tool to investigate the physical mechanisms of large droplet electrodeformations, and offers insights not available from the numerical models.

1.3 Electrohydrodynamic deformation of vesicles

Similar to droplets, vesicles also deform due to charge accumulation. In addition, in this problem, we also need to consider a lipid membrane, and incorporate its effects with a membrane-charging and a membrane-mechanical model. Vesicles are widely used as a model system for biological cells due to their simplicity and controllability. The deformation of the lipid membrane, in particular under an applied electric field (electrodeformation), is often explored to probe membrane properties [35, 53] and to detect pathological changes in cells [83].

In the past decade, vesicle electrodeformation has become a significant subject of study, and earlier work can be divided into two categories. In the first category, an alternating-current (AC) field is applied, which often induces stationary and small deformations [3, 15, 35, 53]. Correspondingly, an electrohydrodynamic theory in the small-deformation limit was developed to interpret the data trends [81]. In the second, under DC electric fields, vesicles usually exhibit large and transient deformations due to the large field strengths commonly applied [31, 62, 63, 64]. Recently, using high-resolution, high-speed optical imaging Riske and Dimova [62] acquired a large amount of data capturing the complex deformation-relaxation behavior of the vesicles. Although some qualitative and scaling arguments were presented [15], the data was not fully interpreted due to the absence of a predictive model. Meanwhile, Sadik and co-authors [64] experimentally examined vesicles in the large-deformation regime with aspect ratios reaching ten. A large-deformation theory was also presented, which provided quantitative agreement with the data therein. However, the model was semi-empirical in that the hydrodynamic problem was not rigorously treated, but followed an empirical approach by Hyuga and co-authors [29, 30]. In general, a rigorous and transient analysis needs to be developed to understand the complex deformation-relaxation behavior, and to provide insights on the underlying physical processes.

In this work, we develop a transient analysis for vesicle electrodeformation. The theory is derived by extending our droplet model, with the additional consideration of a lipid membrane separating two fluids of arbitrary properties. For the latter, both a membrane-charging and a membrane-mechanical model are supplied. Similar to the droplet model, the main result is also an ODE governing the evolution of the vesicle aspect ratio. The effects of initial membrane tension and pulse length are examined. The model prediction is extensively compared with experimental data from Riske and Dimova [62] and Sadik *et al.* [64], and is shown to accurately capture the system behavior in the regime of no or weak electroporation. More importantly, the comparison reveals that vesicle relaxation obeys a universal behavior, and is governed by a single timescale that is a function of the vesicle initial radius, the fluid viscosity, and the initial membrane tension. This behavior is regardless of the means of deformation, either via AC/DC electric field, or via mechanical stretching. This universal scaling law is a main contribution of the current work, and can be used to calculate membrane properties from experimental data.

Chapter 2

A General Analysis for The Electrohydrodynamic Instability of Stratified Immiscible Fluids

2.1 Introduction

In this chapter, we present an analysis for the EHD instability of immiscible stratified fluids. Different from previous approaches, which solve the linearized problem for each specific case, we generalized the solution method by directly employing the 'transfer relations' relating interfacial disturbance stresses to disturbance flow variables. The concept for these relations was first introduced by J. R. Melcher [27, 28, 87], and the complete form is found in his classical text [44]. The broad utility of these relations, however, does not seem to have been widely appreciated. Only the hydrodynamic (but not the electrical) transfer relations has been used to analyze a three-layer channel flow in the limit of an infinite conductivity ratio [86]. Here we extend from this work by utilizing both hydrodynamic and electrical transfer relations. We assume that the fluids have arbitrary properties such as viscosity, permittivity, and conductivity without making any idealizations. We will first introduce the method using an exemplary two-layer configuration then we extend the analysis to a three layer geometry. The results are generalized dispersion relations previously not available and include many those from earlier work as special limiting cases. This work has been published in Journal of Fluid Mechanics [88].

2.2 Theory

The schematics of two generic problem configurations are shown in figure 2.1. In figure 2.1(a), two fluid layers (denoted by 1 and 2) of thickness a and b are placed in a straight channel. The interfacial position is denoted by ζ. In figure 2.1(b), an additional layer (fluid 3) is considered, and is assumed to have identical properties as fluid 1. The upper and lower interfacial positions are denoted by ζ_u and ζ_l, respectively. The governing equations for each layer are the incompressible Navier-Stokes equation and the Ohmic equation for current conservation:

$$\rho_j\left(\frac{\partial \boldsymbol{v}_j}{\partial t}+\boldsymbol{v}_j\cdot\nabla\boldsymbol{v}_j\right)=-\nabla p_j+\mu_j\nabla^2\boldsymbol{v}_j, \qquad \nabla\cdot\boldsymbol{v}_j=0, \tag{2.1}$$

$$\nabla\cdot\sigma_j\nabla\phi_j=0. \tag{2.2}$$

Here the subscript j ($j=1$, 2 for the two-layer, and 1, 2, 3 for the three-layer problem, respectively) denotes each fluid layer. ρ, $\boldsymbol{v}$, p, μ, and ϕ are the fluid density, velocity, pressure, viscosity, and the electric potential, respectively. We assume instantaneous charge relaxation such that (2.2) is applicable. The electrical conductivity, σ, and the permittivity, ϵ, of each layer remain constant. A potential $\phi=\phi_o$ is applied at the lower channel wall, and the upper wall is grounded. This arrangement leads to an applied field normal to the undisturbed fluid interface(s). The velocities obey the no-slip condition on the walls. The following interfacial jump conditions are prescribed:

$$||\nabla\phi\cdot\boldsymbol{t}||=0, \quad ||\sigma\nabla\phi\cdot\boldsymbol{n}||=0, \quad ||\boldsymbol{v}||=0, \quad ||\tau\cdot\boldsymbol{n}||+\gamma(\nabla\cdot\boldsymbol{n})\boldsymbol{n}=0. \tag{2.3}$$

Here $||\cdot||$ denotes a jump across an interface, γ is the surface tension coefficient, and $\boldsymbol{t}$ and $\boldsymbol{n}$ are the unit tangential and normal interfacial vector, respectively. The tensor τ includes contributions from both the hydrodynamic and electrostatic stresses:

$$\tau\equiv -p\mathrm{I}+\mu(\nabla\boldsymbol{v}+\nabla\boldsymbol{v}^T)+\epsilon\boldsymbol{E}\boldsymbol{E}-\frac{1}{2}\epsilon(\boldsymbol{E}\cdot\boldsymbol{E})\mathrm{I}, \tag{2.4}$$

where I is the unit tensor, and $\boldsymbol{E}=-\nabla\phi$ is the electric field.

In what follows, we first solve the two-layer problem (figure 2.1a) to illustrate the solution process; the results for the three-layer problem (figure 2.1b) then follow in a straightforward manner. We perform a temporal linear stability analysis using the

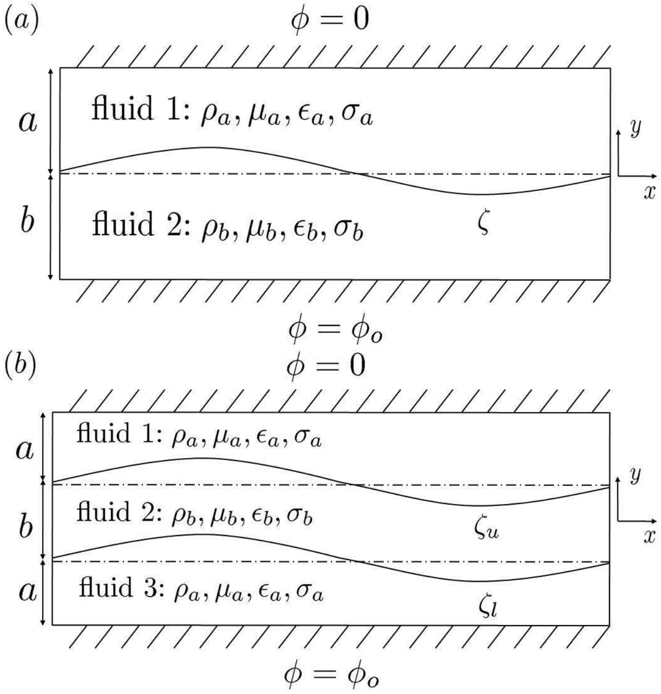
(a)
$\phi = 0$
a
fluid 1: $\rho_a, \mu_a, \epsilon_a, \sigma_a$
y
x
b
fluid 2: $\rho_b, \mu_b, \epsilon_b, \sigma_b$
ζ
$\phi = \phi_o$
(b)
$\phi = 0$
a
fluid 1: $\rho_a, \mu_a, \epsilon_a, \sigma_a$
y
b
fluid 2: $\rho_b, \mu_b, \epsilon_b, \sigma_b$
x
ζ_u
a
fluid 3: $\rho_a, \mu_a, \epsilon_a, \sigma_a$
ζ_l
$\phi = \phi_o$

Figure 2.1: Schematics of the two generic problem configurations.

following decomposition:

$$f = f_o + \hat{f}(y) \exp(ikx + st), \tag{2.5}$$

where f is a generic flow variable, f_o is the base (undisturbed) state, $\hat{f}$ is the complex disturbance amplitude, k is the wavenumber, and s is the growth rate. We assume that the base flow is quiescent, $\boldsymbol{v}_{o,j} = 0$. This assumption is required by the applicability of the transfer relations, and does not affect the generality of the analysis (see §2.3.2). The undisturbed electric fields (aligned in the y-direction) are:

$$E_{o,1} = E_{app}(n+1)/(n+\sigma_r), \quad E_{o,2} = \sigma_r E_{o,1}, \tag{2.6a}$$

$$E_{app} = \phi_o/(a+b), \quad n \equiv a/b, \quad \sigma_r \equiv \sigma_a/\sigma_b. \tag{2.6b}$$

Equations (2.1-2.3) can be linearized using the decomposition (2.5). The results are

$$\left(D_y^2 - k^2\right) \hat{\phi}_j = 0, \tag{2.7}$$

$$\left(D_y^2-\delta_j^2\right)\left(D_y^2-k^2\right)\hat{\psi}_j=0, \quad \delta\equiv\left[k^2+\frac{s\rho}{\mu}\right]^{\frac{1}{2}}, \tag{2.8}$$

$$\hat{\phi}_1^\alpha=\hat{\phi}_2^\beta=0, \quad \sigma_r D_y\hat{\phi}_1^\beta=D_y\hat{\phi}_2^\alpha, \quad -E_{o,1}\hat{\zeta}+\hat{\phi}_1^\beta=-E_{o,2}\hat{\zeta}+\hat{\phi}_2^\alpha, \tag{2.9}$$

$$\hat{u}_1^\alpha=\hat{v}_1^\alpha=\hat{u}_2^\beta=\hat{v}_2^\beta=0, \quad \hat{u}_1^\beta=\hat{u}_2^\alpha=\hat{u}, \quad \hat{v}_1^\beta=\hat{v}_2^\alpha=s\hat{\zeta}, \tag{2.10}$$

$$\hat{T}_{yy1}^\beta-\hat{T}_{yy2}^\alpha+\hat{S}_{yy1}^\beta-\hat{S}_{yy2}^\alpha-\gamma k^2\hat{\zeta}=0, \tag{2.11}$$

$$\hat{T}_{yx1}^\beta-\hat{T}_{yx2}^\alpha+\hat{S}_{yx1}^\beta-\hat{S}_{yx2}^\alpha=0. \tag{2.12}$$

Here D_y is a derivative with respect to y, $\hat{\psi}$ is a stream function which relates to the velocities as $(D_y\hat{\psi},\, -ik\hat{\psi})=(\hat{u},\, \hat{v})$, $\hat{T}$ and $\hat{S}$ denote the hydrodynamic and electrostatic stresses, and the superscripts α and β denote an evaluation at the upper and lower boundary of the fluid layer (1 or 2), respectively. In general, an analytical solution of this linear system can be pursued, and the results are expressed in terms of hyperbolic functions. An eigenvalue problem is then formulated to solve for s, the growth rate, and the array of coefficients for the hyperbolic functions form the corresponding eigenvector (see, e.g. [47, 57]). In the present work, we adopt an alternative, convenient approach employing the transfer relations by Melcher [44]. For a generic fluid layer with density ρ, viscosity μ, and a thickness $\triangle$, the transfer relations read

$$\begin{bmatrix} -D_y\hat{\phi}^\alpha \\ -D_y\hat{\phi}^\beta \end{bmatrix}=k\begin{bmatrix} -\coth(k\triangle) & \operatorname{csch}(k\triangle) \\ -\operatorname{csch}(k\triangle) & \coth(k\triangle) \end{bmatrix}\begin{bmatrix} \hat{\phi}^\alpha \\ \hat{\phi}^\beta \end{bmatrix}, \tag{2.13}$$

$$\begin{bmatrix} \hat{T}_{yy}^\alpha \\ \hat{T}_{yy}^\beta \\ \hat{T}_{yx}^\alpha \\ \hat{T}_{yx}^\beta \end{bmatrix}=\begin{bmatrix} A & B & iC & iD \\ -B & -A & iD & iC \\ -iC & iD & E & F \\ iD & -iC & -F & -E \end{bmatrix}\begin{bmatrix} \hat{v}^\alpha \\ \hat{v}^\beta \\ \hat{u}^\alpha \\ \hat{u}^\beta \end{bmatrix}. \tag{2.14}$$

Evidently, these relations relate the interfacial disturbance electric fields and hydrodynamic stresses to the disturbance flow variable amplitudes $(\hat{\phi},\, \hat{u},\, \hat{v})$. These relations are general properties of the system (2.7), (2.8), *independent* of the boundary matching conditions (2.9-2.12). In other words, they are valid regardless of the specific boundary values. The 'transfer coefficients' $A-F$ are combinations of hyperbolic functions,

$$A = \frac{-\mu(\delta^2 - k^2)}{kG}\left(\frac{k}{\delta}\coth(\delta\Delta) - \coth(k\Delta)\right), \tag{2.15}$$

$$B = \frac{\mu(\delta^2 - k^2)}{kG}\left(\frac{k}{\delta}\text{csch}(\delta\Delta) - \text{csch}(k\Delta)\right), \tag{2.16}$$

$$C = -\frac{\mu}{G}\left[\delta\left(1 + \frac{3k^2}{\delta^2}\right)(\text{csch}(k\Delta)\text{csch}(\delta\Delta) - \coth(k\Delta)\coth(\delta\Delta)) + k\left(3 + \frac{k^2}{\delta^2}\right)\right], \tag{2.17}$$

$$D = \frac{\mu(\delta^2 - k^2)}{\delta G}(\coth(\delta\Delta)\text{csch}(k\Delta) - \coth(k\Delta)\text{csch}(\delta\Delta)), \tag{2.18}$$

$$E = \frac{-\mu(\delta^2 - k^2)}{\delta G}\left(\frac{k}{\delta}\coth(k\Delta) - \coth(\delta\Delta)\right), \tag{2.19}$$

$$F = \frac{-\mu(\delta^2 - k^2)}{\delta G}\left(\text{csch}(\delta\Delta) - \frac{k}{\delta}\text{csch}(k\Delta)\right), \tag{2.20}$$

$$G \equiv 1 + \frac{k^2}{\delta^2} + \frac{2k}{\delta}(\text{csch}(k\Delta)\text{csch}(\delta\Delta) - \coth(k\Delta)\coth(\delta\Delta)), \tag{2.21}$$

where G is a common denominator shared by all coefficients, and δ is defined in (2.8). A brief explanation of the derivation of the transfer relations is found in Appendix A. Interested readers are referred to Melcher (1981, §2.16, §7.19) for further details. Note that our definitions of C and D differ from those by Melcher by a factor of i. This convenient change ensures that all coefficients in the final results (2.26), (2.33), (2.34) are real if s itself is real. Equation (2.13) holds regardless of the orientation of the applied field. If we further consider a normal applied field, E_o, the disturbance magnitudes of the electrostatic stress, $\hat{S}$, can be expressed as

$$\hat{S}_{yy} = -\epsilon E_o D_y \hat{\phi}, \quad \hat{S}_{yx} = ik\epsilon E_o(E_o\hat{\zeta} - \hat{\phi}). \tag{2.22}$$

With the help of (2.13), we can construct a transfer relation between $\hat{S}$ and $\hat{\phi}$, $\hat{\zeta}$:

$$\begin{bmatrix} \hat{S}^{\alpha}_{yy} \\ \hat{S}^{\beta}_{yy} \\ \hat{S}^{\alpha}_{yx} \\ \hat{S}^{\beta}_{yx} \end{bmatrix} = k\epsilon E_o \begin{bmatrix} -\coth(k\triangle) & \operatorname{csch}(k\triangle) & 0 & 0 \\ -\operatorname{csch}(k\triangle) & \coth(k\triangle) & 0 & 0 \\ -i & 0 & iE_o & 0 \\ 0 & -i & 0 & iE_o \end{bmatrix} \begin{bmatrix} \hat{\phi}^{\alpha} \\ \hat{\phi}^{\beta} \\ \hat{\zeta}^{\alpha} \\ \hat{\zeta}^{\beta} \end{bmatrix}. \tag{2.23}$$

Note that (2.23) is specific to the configuration of a normal applied field due to the dependence of (2.22) on the base state. A similar relation for a parallel applied field can also be derived (not shown here). The availability of (2.14), (2.23) enables a straightforward and systematic solution method of the normal-mode problem, following the steps below. First, (2.9), (2.10) are used to reduce the independent disturbance variables to two, namely, $\hat{\zeta}$ and $\hat{u}$, where $\hat{u}$ is the interfacial streamwise velocity defined in (2.10). Note that in doing so, we also use the transfer relation (2.13) to eliminate the derivatives in favor of the potentials in (2.9). In the next step, (2.14), (2.23) are used to evaluate the stress conditions (2.11), (2.12). For example, the first term in (2.11) can be expressed with the help of (2.14) as

$$\hat{T}^{\beta}_{yy1} = -B_a\hat{v}^{\alpha}_1 - A_a\hat{v}^{\beta}_1 + iD_a\hat{u}^{\alpha}_1 + iC_a\hat{u}^{\beta}_1 = -A_a s\hat{\zeta} + iC_a\hat{u}, \tag{2.24}$$

where a subscript a implies that $A - F$ are evaluated with the properties of fluid 1 (ρ_a, μ_a, and thickness a), and we have used (2.10), namely, $\hat{u}^{\alpha}_1 = \hat{v}^{\alpha}_1 = 0$. The final results are assembled in a matrix format to yield:

$$\begin{bmatrix} -(A_a + A_b)s + Q_N g - \gamma k^2 & i\,(C_a - C_b) \\ -i(C_a - C_b)s + iQ_T h & -(E_a + E_b) \end{bmatrix} \begin{bmatrix} \hat{\zeta} \\ \hat{u} \end{bmatrix} = 0, \tag{2.25a}$$

$$Q_N = k\epsilon_b E^2_{o,1}(\sigma_r - 1)(\sigma^2_r - \epsilon_r), \quad Q_T = k\epsilon_b E^2_{o,1}\sigma_r\,(\epsilon_r - \sigma_r)\,, \quad \epsilon_r \equiv \epsilon_a/\epsilon_b, \tag{2.25b}$$

$$g = \frac{1}{\tanh(ka) + \sigma_r \tanh(kb)}, \quad h = \frac{\tanh(ka) + \tanh(kb)}{\tanh(ka) + \sigma_r \tanh(kb)}. \tag{2.25c}$$

Similarly, $A_b - F_b$ are the resulting coefficients for fluid 2. The factors Q_T and Q_N arise from the effects of the tangential and normal electrical stresses, respectively, and our notations follow those of Li *et al.* [39]. They are important in predicting the stabilizing/destabilizing effects of these stresses, which we further discuss below. The dispersion relation is obtained by requiring the matrix to be singular:

$$(C_a - C_b)\left[-(C_a - C_b)s + Q_T h\right] + (E_a + E_b)\left[(A_a + A_b)s - Q_N g + \gamma k^2\right] = 0. \quad (2.26)$$

The growth rate s can be solved given a wavenumber k.

The solution of the three-layer problem follows the same approach. The details are not presented. The resulting matrix format of the stress conditions is

$$\begin{bmatrix} -(A_a + A_b)s + Q_N g_1 - \gamma k^2 & -B_b s + Q_N h_1 & i\,(C_a - C_b) & -iD_b \\ -B_b s + Q_N h_1 & -(A_a + A_b)s + Q_N g_1 - \gamma k^2 & iD_b & -i(C_a - C_b) \\ -i(C_a - C_b)s + iQ_T g_2 & -(iD_b s - iQ_T h_2) & -(E_a + E_b) & -F_b \\ iD_b s - iQ_T h_2 & i(C_a - C_b)s - iQ_T g_2 & -F_b & -(E_a + E_b) \end{bmatrix}$$

$$\begin{bmatrix} \hat{\zeta}_u \\ \hat{\zeta}_l \\ \hat{u}_u \\ \hat{u}_l \end{bmatrix} = 0. \quad (2.27)$$

Here the four rows represent the normal and tangential stress conditions at the upper (ζ_u) and lower (ζ_l) interfaces, respectively. $\hat{u}_u$ and $\hat{u}_l$ are the interfacial streamwise disturbance velocities, also at $y = \zeta_u,\ \zeta_l$. Similar to the two-layer problem, all other disturbance variables are eliminated in favor of these four, using continuity conditions at the interfaces. The coefficients of $A - F$, Q_T and Q_N assume the same definitions as in (2.15-2.20) and (2.25b). However, note that now $E_{o,1}$ has a different value for the three-layer problem, namely, $E_{o,1} = \phi_o/\left(2a + b\sigma_r\right)$ instead. $g_{1,2}$ and $h_{1,2}$ are similar to g and h, and are given by the following expressions:

$$g_1 = [\tanh(ka)\sinh(kb) + \sigma_r \cosh(kb)]/H_o, \quad (2.28)$$

$$h_1 = -\sigma_r/H_o, \quad (2.29)$$

$$g_2 = [(\tanh^2(ka) + \sigma_r)\sinh(kb) + (\sigma_r + 1)\tanh(ka)\cosh(kb)]/H_o, \tag{2.30}$$

$$h_2 = -(\sigma_r - 1)\tanh(ka)/H_o, \tag{2.31}$$

$$H_o = (\tanh^2(ka) + \sigma_r^2)\sinh(kb) + 2\sigma_r\tanh(ka)\cosh(kb). \tag{2.32}$$

The eigenvalue problem gives rise to two branches of dispersion relations:

$$\begin{aligned}&(C_a - C_b + D_b)[-(C_a - C_b + D_b)s + Q_T(g_2 + h_2)]\\&+(E_a + E_b - F_b)[(A_a + A_b + B_b)s - Q_N(g_1 + h_1) + \gamma k^2] = 0,\end{aligned} \tag{2.33}$$

$$\begin{aligned}&(C_a - C_b - D_b)[-(C_a - C_b - D_b)s + Q_T(g_2 - h_2)]\\&+(E_a + E_b + F_b)[(A_a + A_b - B_b)s - Q_N(g_1 - h_1) + \gamma k^2] = 0.\end{aligned} \tag{2.34}$$

The corresponding eigenvectors are

$$[1,\ 1,\ \lambda_K,\ -\lambda_K]^T, \quad [1,\ -1,\ \lambda_S,\ \lambda_S]^T, \tag{2.35}$$

where λ_K and λ_S are constants. The first eigenmode yields a wavy, sinusoidal pattern where the interfaces are in-phase ($\hat{\zeta}_u = \hat{\zeta}_l$). We term this mode 'kink' following one of us [86]. In the second mode, the interfaces deform symmetrically with respect to the centerline ($\hat{\zeta}_u = -\hat{\zeta}_l$), which we term 'sausage'. Typical streamlines are shown in figure 2.2. Note that the two modes directly arise from the eigenvalue problem (2.27), whereas in both [49] and [57], an *a priori* symmetry or anti-symmetry was assumed. Equations (2.26), (2.33), (2.34) are the main results of the current analysis.

We remark that the above solution approach has several important advantages. First, formulating the eigenvalue problem in terms of the disturbance variables ($\hat{\phi}, \hat{\zeta}, \hat{u}, \hat{v}$) is more physical than in terms of the algebraic coefficients (e.g. in [47]). The eigenmodes yield clear physical meanings in this formulation. Second, the approach provides a systematic treatment for a generic class of problems. We emphasize that obtaining the transfer relations is indeed equivalent to solving the linear problem as pursued by

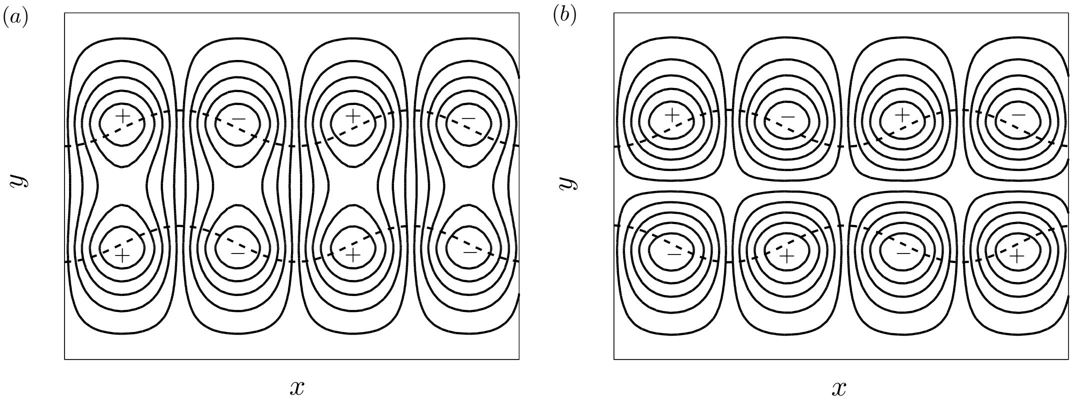

Figure 2.2: Typical streamline patterns for the (a) kink and (b) sausage mode of the three-layer problem. The dashed lines denote the interfacial positions. A '+' or '−' sign denotes a local maximum or minimum of the stream function, respectively.

previous authors. However, once they are available, they can be immediately applied to assemble the eigenvalue problem. Last but not least, the results assume broad generality. Below we show that both new dispersion relations and those from prior work can be obtained as special cases of our general solution by considering proper simplifications.

2.3 Specific cases

2.3.1 Two semi-infinite layers ($a,\ b \to \infty$)

We first show that the result for two semi-infinite layers can be obtained by simply taking the limit of $a,\ b \to \infty$ in the coefficients in (2.26):

$$\left(C_a^\infty - C_b^\infty\right)\left[-\left(C_a^\infty - C_b^\infty\right)s + Q_T h^\infty\right] + \left(E_a^\infty + E_b^\infty\right)\left[\left(A_a^\infty + A_b^\infty\right)s - Q_N g^\infty + \gamma k^2\right] = 0, \tag{2.36a}$$

$$A^\infty = \mu\delta\left(\delta + k\right)/k, \quad C^\infty = \mu\left(\delta - k\right), \quad E^\infty = \mu\left(\delta + k\right), \tag{2.36b}$$

$$g^\infty = 1/\left(1 + \sigma_r\right), \quad h^\infty = 2g^\infty. \tag{2.36c}$$

The transfer coefficients A^∞, C^∞, E^∞ are noticeably simplified in their expressions. However, they still do depend on the specific fluid properties, namely, ρ and μ. This configuration was first studied by Melcher [47] without assuming an instantaneous charge relaxation. Equation (2.36a) agrees with (19) therein if the proper limits of ϵ_a/σ_a, $\epsilon_b/\sigma_b \to 0$ are taken in the latter equation. In general (2.36a) has a complex dependence on s through the variable δ in the coefficients (see (2.8)). An explicit expression for s, however, can be obtained by further considering the zero-Reynolds-number limit. Here due to the absence of an apparent velocity scale, we define the Reynolds number as

$$Re \equiv \rho s/\mu k^2. \tag{2.37}$$

With this definition, a small Reynolds number means that the viscous diffusion time, $\rho/\mu k^2$, is much smaller than the instability time, $1/s$. Evaluating (2.36a) in the limit of $Re \to 0$ yields

$$s = \left(Q_N g^\infty - \gamma k^2\right)/2k(\mu_a + \mu_b). \tag{2.38}$$

When compared with (2.36a), the most important feature of (2.38) is that the effect of the tangential electrical stress (Q_T) disappears, and the stability completely depends on the balance between the normal electrical stress (Q_N) and the surface tension. The latter is always stabilizing, whereas the former may stabilize or destabilize the flow depending on the sign of Q_N, or equivalently, $(\sigma_r - 1)(\sigma_r^2 - \epsilon_r)$. A sufficient (but not necessary) condition for stability is found for $(\sigma_r - 1)(\sigma_r^2 - \epsilon_r) < 0$. In general, in the limit of $Re \to 0$, an explicit expression for s is always attainable. Similar situations are found below.

2.3.2 Two finite layers

This configuration is of great interest to microfluidic applications where the liquids are confined in a channel. Note that equation (2.26) presents a general dispersion relation for an arbitrary Reynolds number, and is one of the new results generated by this work. To consider the solution in the zero-Reynolds-number limit, we evaluate $A - F$ in (2.26) in the limit of $\rho s/\mu k^2 \to 0$. We denote the resulting coefficients by $A^0 - F^0$,

$$A^0 = 2\mu k\left[\coth(k\triangle) + \operatorname{csch}^2(k\triangle)k\triangle\right]/\left[1 - \operatorname{csch}^2(k\triangle)\left(k\triangle\right)^2\right], \tag{2.39}$$

$$B^0 = \frac{-2\mu k\left[\operatorname{csch}(k\triangle) + \coth(k\triangle)\operatorname{csch}(k\triangle)k\triangle\right]}{1 - \operatorname{csch}^2(k\triangle)\,(k\triangle)^2}, \tag{2.40}$$

$$C^0 = \frac{2\mu k^3\triangle^2\operatorname{csch}^2(k\triangle)}{1 - \operatorname{csch}^2(k\triangle)\,(k\triangle)^2}, \tag{2.41}$$

$$D^0 = \frac{2\mu k^2\triangle\operatorname{csch}(k\triangle)}{1 - \operatorname{csch}^2(k\triangle)\,(k\triangle)^2}, \tag{2.42}$$

$$E^0 = \frac{-2\mu k\left[\operatorname{csch}^2(k\triangle)k\triangle - \coth(k\triangle)\right]}{1 - \operatorname{csch}^2(k\triangle)\,(k\triangle)^2}, \tag{2.43}$$

$$F^0 = \frac{2\mu k\left[\coth(k\triangle)\operatorname{csch}(k\triangle)k\triangle - \operatorname{csch}(k\triangle)\right]}{1 - \operatorname{csch}^2(k\triangle)\,(k\triangle)^2}. \tag{2.44}$$

The coefficients Q_T, Q_N, g, and h are not affected by this evaluation. We immediately note that $A^0 - F^0$ no longer depend on s because $\delta \to k$. An explicit solution for s is obtained as

$$s = \frac{\left(E_a^0 + E_b^0\right)\left(Q_N g - \gamma k^2\right) - \left(C_a^0 - C_b^0\right)Q_T h}{\left(E_a^0 + E_b^0\right)\left(A_a^0 + A_b^0\right) - \left(C_a^0 - C_b^0\right)^2}. \tag{2.45}$$

In general, both the tangential and normal electrical stresses contribute to the growth rate, as indicated by the presence of Q_T and Q_N. The influence of the tangential stress disappears if we further assume $\mu_a = \mu_b$, and $a = b$, such as to recover the results by Uguz *et al.* [78]. This simplification sets $C_a^0 - C_b^0$ to zero, and (2.45) becomes

$$s = \left(Q_N g - \gamma k^2\right)/2A_a^0. \tag{2.46}$$

Equation (2.46) shares similarity with (2.38), in that the stability is completely determined by the balance between the normal electrical stress and the surface tension. This case has been studied in great detail by Uguz and Aubry (2008, cf. equation (51) therein), and is not further discussed. The result by Thaokar and Kumaran [76] is obtained if (2.46) is evaluated in the limit of $k \to 0$ (cf. equation (46) therein). We remark that when comparing (2.46) with equation (51) in [78], we find that the addition of a non-uniform base flow (which is present in [78], but not in the current analysis) only induces a simple convection which manifests itself in the imaginary part of the growth rate. The base flow can have a more complex effect on the growth rate for the case of $Re \neq 0$. For example, Li *et al.* [39] performed a long-wave analysis with a finite

Re. The results show that the non-uniform base flow also affects the real part of the growth rate in the first-order correction term.

2.3.3 Three layers, infinite domain ($a \to \infty$)

This problem was first considered by Michael and O'Neill [49], where an insulating fluid was sandwiched in between two conducting fluids of semi-infinite geometry ($\sigma_r \to \infty$, $n \to \infty$), and was subject to a normal applied field. A more recent work by [57] considered the same geometry, but with a parallel field, and the fluids were assumed to have arbitrary permittivity and conductivity values. In both of the studies, symmetry ($\hat{\zeta}_u = \hat{\zeta}_l$) or anti-symmetry ($\hat{\zeta}_u = -\hat{\zeta}_l$) was assumed *a priori* in the analysis. Here as we have demonstrated above, these two modes arise naturally from the eigenvalue problem (2.27). In fact, should the properties of fluid 3 differ from those of fluid 1, the symmetry/anti-symmetry will break, and the upper and lower interfaces may grow/decay with a relative phase angle other than 0 or π. The dispersion relations for this geometry with a normal applied field can be achieved by simply replacing A_a, C_a, E_a with A_a^∞, C_a^∞, E_a^∞ (defined in (2.36b)), and $g_{1,2}$, $h_{1,2}$ with $g_{1,2}^\infty$, $h_{1,2}^\infty$:

$$g_1^\infty = \frac{\tanh(kb) + \sigma_r}{(1+\sigma_r^2)\tanh(kb) + 2\sigma_r}, \tag{2.47}$$

$$g_2^\infty = \frac{(1+\sigma_r)\left[\tanh(kb) + 1\right]}{(1+\sigma_r^2)\tanh(kb) + 2\sigma_r}, \tag{2.48}$$

$$h_1^\infty = \frac{-\sigma_r}{(1+\sigma_r^2)\sinh(kb) + 2\sigma_r\cosh(kb)}, \tag{2.49}$$

$$h_2^\infty = \frac{1-\sigma_r}{(1+\sigma_r^2)\sinh(kb) + 2\sigma_r\cosh(kb)}. \tag{2.50}$$

The result is a simple notation change from (2.33), (2.34), and is not presented here. Note that this result is new due to an arbitrary σ_r, in contrast to the limit of $\sigma_r \to \infty$ considered by Michael and O'Neill [49] for a normal field. To recover the latter, we take this limit for Q_T, Q_N, $g_{1,2}^\infty$, and $h_{1,2}^\infty$ to yield:

$$Q_N\left(g_1^\infty \pm h_1^\infty\right)|_{\sigma_r\to\infty} = k\epsilon_b\left(\phi_o/b\right)^2\left[\coth(kb) \mp \operatorname{csch}(kb)\right], \tag{2.51}$$

$$Q_T\left(g_2^\infty \pm h_2^\infty\right)|_{\sigma_r \to \infty} = 0. \tag{2.52}$$

These terms are the only ones affected by a change in σ_r. The effect of tangential electrical stress disappears again, and the dispersion relations become equation (5.23) in Michael and O'Neill [49] (presented in Appendix B). Following the same procedure and considering a parallel field instead, the result by Papageorgiou and Petropoulos [57] can also be obtained, which we do not show.

2.3.4 Three finite layers

This flow configuration is also commonly adopted in microfluidic applications for fluid handling or mixing purposes. For this case equations (2.33), (2.34) provide the general dispersion relations for the two modes under a normal applied field, and are the most significantly new results from the current work. In the special case of $\sigma_r \to \infty$, which is a finite-depth counterpart to that considered by [49] in an infinite domain, (2.33), (2.34) recover (77) in [86]. The resulting limiting values for the factors $Q_N(g_1 \pm h_1)$ and $Q_T(g_2 \pm h_2)$ are the same as in (2.51), (2.52), although a is finite in this case. (In deriving (2.51), (2.52), $a \to \infty$ has been assumed.)

In the next section, we further investigate in detail the instability behavior for this flow configuration, and provide a comprehensive characterization based on the analytical results.

2.4 Instability behavior for a three-layer channel flow

2.4.1 The zero-Reynolds-number limit ($Re \to 0$)

As demonstrated above, explicit expressions for the growth rate can be obtained in this limit due to the decoupling of s from the transfer coefficients $A - F$. The availability of these expressions helps to illustrate the general characteristics of the instability. Without losing generality, we also assume $\mu_a = \mu_b$, and $a = b$. The dispersion relations as derived from (2.33), (2.34), after considering $\rho s/\mu k^2 \to 0$, read:

$$s^K = \frac{-D_a^0 Q_T (g_2 + h_2) + \left(2E_a^0 - F_a^0\right) Q_N (g_1 + h_1) - \left(2E_a^0 - F_a^0\right)\gamma k^2}{-\left(D_a^0\right)^2 + \left(2E_a^0 - F_a^0\right)\left(2A_a^0 + B_a^0\right)}, \tag{2.53}$$

$$s^S = \frac{D_a^0 Q_T (g_2 - h_2) + \left(2E_a^0 + F_a^0\right) Q_N (g_1 - h_1) - \left(2E_a^0 + F_a^0\right)\gamma k^2}{-\left(D_a^0\right)^2 + \left(2E_a^0 + F_a^0\right)\left(2A_a^0 - B_a^0\right)}, \tag{2.54}$$

where the superscripts K and S denote the kink and sausage mode, respectively. In general both the tangential and normal electrical stresses contribute to the stability (shown by the presence of Q_T and Q_N). Furthermore, it is straightforward to verify that all coefficients D_a^0, $2E_a^0 \pm F_a^0$, $2A_a^0 \pm B_a^0$, $g_1 \pm h_1$, $g_2 \pm h_2$, and the denominators are positive for all wavenumbers. The signs of Q_T and Q_N therefore solely determine the stabilizing or destabilizing behavior of the stresses they respectively represent. Due to the simple dependence of Q_T and Q_N on σ_r, ϵ_r, the evaluation is straightforward. The results are summarized in figure 2.3. In the plots, T denotes a region of a destabilizing tangential stress, and N denotes a region of a destabilizing normal stress, in the phase space of σ_r and ϵ_r. It is interesting to note from (2.53), (2.54) that the tangential stress has opposite effects on the kink and sausage mode, due to the sign of the respective terms involving Q_T. The effect of the normal stress is consistent for both modes. Evidently, the flow is the most susceptible to instability if both stresses are destabilizing. On the other hand, if both are stabilizing (the shaded areas in figure 2.3), then it is sufficient to predict stability due to the stabilizing nature of the surface tension. Note that these observations hold true generally regardless of the specific parameters we use (e.g. E_{app}, μ, ρ, etc.). The results above elucidate the importance of the contour lines, namely, $\sigma_r = \epsilon_r$, $\sigma_r^2 = \epsilon_r$, and $\sigma_r = 1$, in demarcating the different regions of stability behavior. Next, we resort to numerical evaluations of (2.33), (2.34) to directly compute the growth rates for arbitrary Reynolds numbers and fluid properties. We will observe that although deviations from the zero-Re behavior are expected, results from figure 2.3 can still serve as a guide to understand the general system behavior.

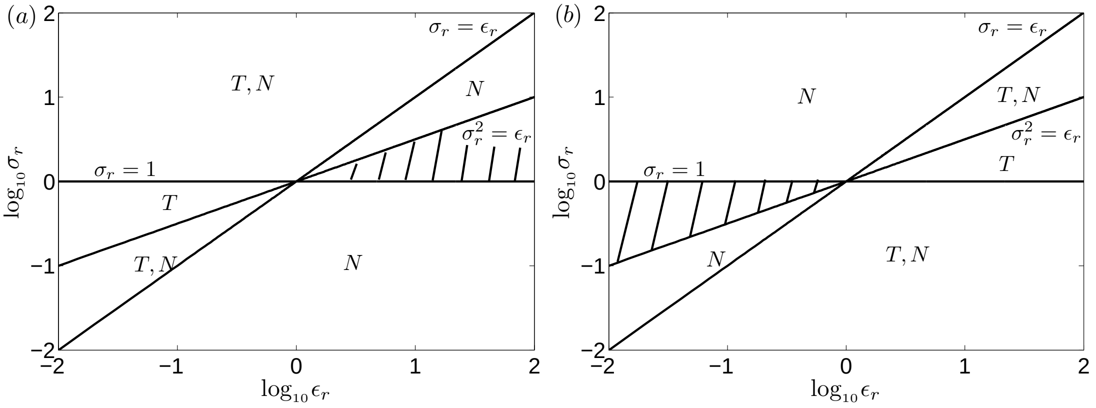

Figure 2.3: Phase diagram for the (a) kink, and (b) sausage mode. Here T denotes a destabilizing tangential stress; and N, a destabilizing normal stress. The shaded areas denote regions of stability where both stresses have stabilizing effects.

2.4.2 Finite Reynolds numbers

We consider the general stability behavior by numerically solving (2.33), (2.34) with generic fluid properties. The input parameters are shown in table 2.1. These parameters are chosen to best approximate the experimental conditions used by Zahn and Reddy [86]. The permittivity ratio, ϵ_r, the conductivity ratio, σ_r, and the electric field strength, E_{app}, are set to be free parameters. The instability behavior with respect to the variations in these three parameters is the main focus of the following study. From equations (2.33), (2.34), the growth rate, s, is generally a complex number for given fluid properties, wavenumber, and electric field strength. We use Muller's method to solve for s numerically.

We begin by examining the behavior of the dispersion curves. In figure 2.4, the real part of the growth rate, s_r, is plotted against the dimensionless wavenumber, kb, at different electric field strengths. For this case, the conductivity and permittivity ratios are chosen to be $\sigma_r = 5$, and $\epsilon_r = 3$, respectively. It is found that for both the kink and sausage modes the electric field has a destabilizing effect. The flow is unstable at low wavenumbers, and stable at high wavenumbers where surface tension dominates. As the field strength increases, the maximum growth rate (denoted by s_{max}) increases. The corresponding wavenumber, k_{max}, also increases. For microfluidic experiments, this result suggests the formation of smaller droplets at higher fields. When compared

Symbol	Description	Value
ρ_a	Density of fluid 1 and 3	10^3 kg/m^3
ρ_b	Density of fluid 2	1.33×10^3 kg/m^3
μ_a	Viscosity of fluid 1 and 3	10^{-3} kg/s $\cdot$ m
μ_b	Viscosity of fluid 2	3.52×10^{-3} kg/s $\cdot$ m
ϵ_b	Permittivity of fluid 2	7.0092×10^{-11} F/m
γ	Surface tension	10^{-4} N/m
a, b	Thicknesses of the fluid layers	50 μm
n	Fluid thickness ratio	1

Table 2.1: List of model parameters. The parameters are chosen following Zahn and Reddy [86].

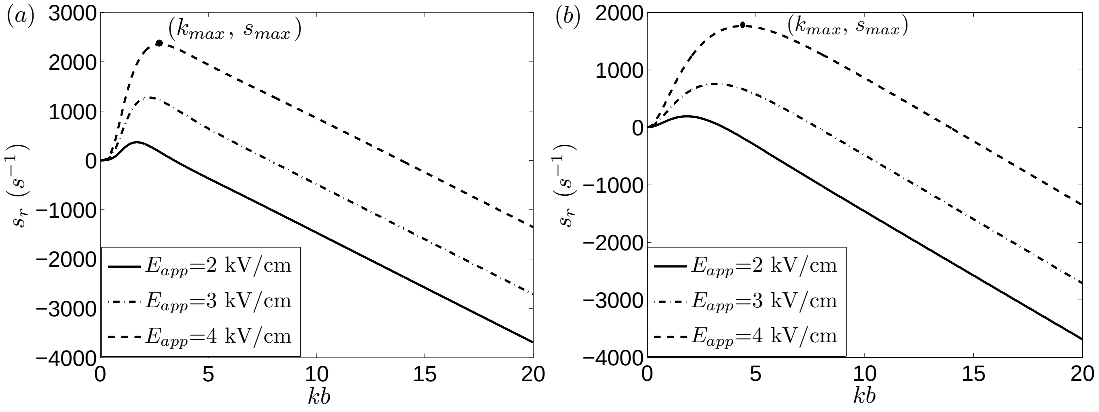

Figure 2.4: The real growth rate as a function of the wavenumber for the (a) kink, and (b) sausage mode. The wavenumber at which the maximum growth rate (s_{max}) occurs is denoted k_{max} (see, e.g. the black dots for E_{app}=4 kV/cm).

against each other, the kink mode is slightly more unstable. This trend can be in part explained using the results for $Re \to 0$ (§2.4.1). For $\sigma_r = 5$, and $\epsilon_r = 3$, the system falls in the upper-left region of the phase space (figure 2.3), where both the tangential and normal stress are destabilizing for the kink mode; whereas for the sausage mode, these two stresses are counter-effective on the growth rate. The kink mode is therefore anticipated to be more unstable. Further quantitative comparison between the two modes are found in figure 2.8 below.

Next, the growth rate is shown in the phase space of σ_r and ϵ_r. Here the contours are of the maximum growth rate, s_{max}, defined in figure 2.4. The applied field strength is $E_{app} = 3$ kV/cm. The neutral stability curves are the zero-value contours, which

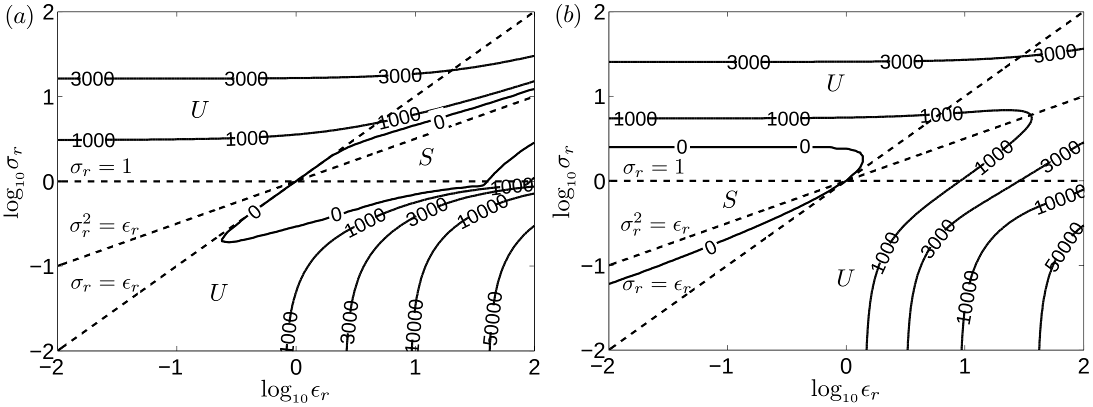

Figure 2.5: Contour plot of the maximum growth rate (s_{max}, in the unit of s^{-1}) for the (a) kink, and (b) sausage mode. Here S denotes a stable region, and U denotes an unstable region.

demarcate the stable (S) and unstable (U) regions. Note that the contours do in part follow the three dividing lines ($\sigma_r = \epsilon_r$, $\sigma_r^2 = \epsilon_r$, and $\sigma_r = 1$, all dashed). In particular, the stability regions contain those noted in figure 2.3, except for a small area in figure 2.5(a) for the kink mode. Two interesting features of figure 2.5 are noteworthy. First, for high values of σ_r, s_{max} is independent of ϵ_r. This is a natural consequence of the fact that for $\sigma_r \to \infty$, $Q_T = 0$, and Q_N no longer depends on ϵ_r (equations (2.51), (2.52), which apply to both infinite and finite values of a). Likewise, at small values of σ_r ($\sigma_r \to 0$), the growth rates are independent of σ_r, and scale approximately linearly with ϵ_r. This trend is again explained by the scaling behavior of Q_N and Q_T. From equation (2.25b) we obtain:

$$Q_N|_{\sigma_r \to 0} = k\epsilon_b E_{o,1}^2 \epsilon_r, \qquad Q_T|_{\sigma_r \to 0} = 0. \tag{2.55}$$

That is, the destabilizing effect of the tangential stress vanishes, and the destabilizing effect of the normal stress scales with ϵ_r.

The corresponding wavenumber, k_{max}, exhibits a similar pattern, as shown in figure 2.6. The independence on ϵ_r for the high-σ_r region, and on σ_r for the low-σ_r region are explained with the same qualitative arguments above. Furthermore, for the unstable regions for both the kink and sausage modes, k_{max} in general scales positively with

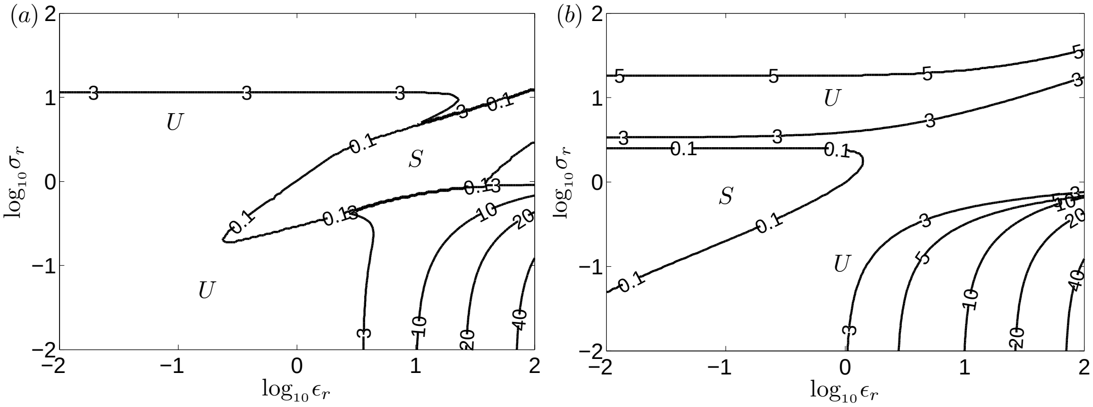

Figure 2.6: Contour plot of the maximum wavenumber (k_{max}) for the (a) kink, and (b) sausage mode.

σ_r and ϵ_r. Most interestingly, by comparing figure 2.6 with figure 2.5, we observe a positive correlation between k_{max} and s_{max}. This observation has important physical implications: a slower mixing between the two fluids (corresponding to a smaller value of s_{max}) produces larger droplets (corresponding to a smaller value of k_{max}), whereas a more rapid mixing produces smaller droplets.

Next, in figure 2.7, we investigate the effects of applied electric field on the neutral stability curves ($s_{max} = 0$). Three field strength, namely, E_{app}=1, 3, and 5 kV/cm, are examined. For both the kink and sausage modes, the stability regions shrink along with an increase in field strength, indicating the overall destabilizing effect for the latter. In comparison, the field strength affects the kink mode more than the sausage mode. The stability region shrinks more slowly for the latter, and always encompasses the predicted stable region in the zero-Re limit (see figure 2.3).

Finally, in figure 2.8, we compare the growth rates for the kink and sausage modes. For a given set of parameters (σ_r, ϵ_r, and E_{app}), although many modes are theoretically unstable, only the one with the fastest growth rate is likely observed experimentally. In figure 2.8(a), the solid curve is obtained by setting equal the maximum growth rate, s_{max}, for the kink and sausage modes ($s^K_{max} = s^S_{max}$). In the domain denoted 'kink dominant', $s^K_{max} > s^S_{max}$, and the kink mode prevails. similarly, the 'sausage dominant' area is determined by the condition $s^K_{max} < s^S_{max}$. Close to the boundary where the

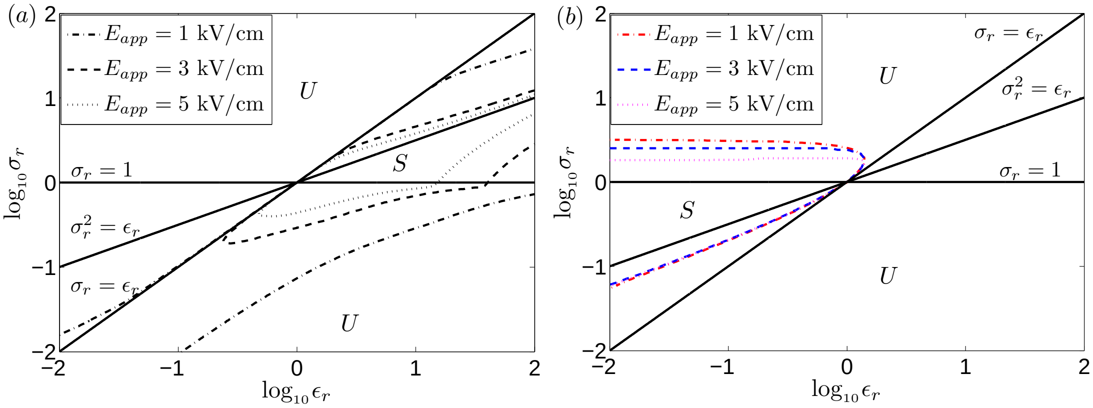

Figure 2.7: The effect of the applied electric field on the neutral stability curve for the (a) kink, and (b) sausage mode. The stable region shrinks as the field strength increases.

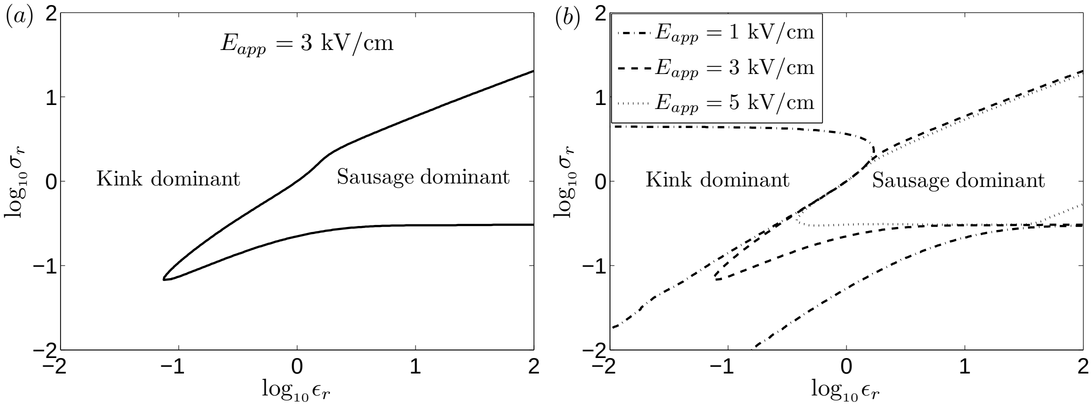

Figure 2.8: (a) Comparison of the maximum growth rate between the kink and sausage modes for E_{app}=3 kV/cm. A kink dominant region suggests that the kink mode grows more rapidly than the sausage mode. (b) An increasing field strength expands the kink-dominant region at the expense of the sausage-dominant region.

		k_{max}		
E_{app} (kV/cm)	Mode	Measured	Current model	ZR2006
2.67	sausage	2.3	5.1	2.2
2.73	sausage	4.1	5.2	2.2
2.80	sausage	5.1	5.4	2.3
2.93	kink	5.5	4.2	2.5
3.00	kink	5.5	4.3	2.5

Table 2.2: Comparison of the wavenumber for the fastest-growing mode, k_{max}, from measurements by Zahn and Reddy (2006, denoted "measured"), the current model, and the prediction via a simplified model assuming $\sigma_r \to \infty$ (also from Zahn and Reddy [86], denoted "ZR2006").

two growth rates equate, and the two modes compete closely with each other, we may observe 'mixed' patterns where both are present and are superimposed on each other. In figure 2.8(b), the effect of the electric field on mode dominance is examined. The general trend reveals that an increased field strength expands the kink-dominant domain.

2.4.3 A comparison with experimental data

For the final part of the study, we compare our theoretical prediction with available experimental data, e.g. from Zahn and Reddy [86]. We choose to compare the fastest-growing wavenumber, k_{max}, as it is the only quantitative measurement provided. The experimental observation determines whether the observed mode is kink or sausage. We then use (2.33), (2.34) to evaluate k_{max}. The results are tabulated in table 2.2. Based on the experimental configuration, we use $\sigma_r = 541$, $\epsilon_r = 11$. Other parameters follow table 2.1. The field strength, E_{app}, varies from 2.67 to 3.00 kV/cm. For comparison, the predicted k_{max} by Zahn and Reddy [86] is also presented, where they assumed $\sigma_r \to \infty$ in the calculation. The results reveal that our prediction very reasonably reproduces the observed values (except for E_{app}=2.67 kV/cm), despite that the model is two-dimensional, whereas the experimental geometry is intrinsically three-dimensional. In contrast, the more idealized prediction from Zahn and Reddy [86] yields a much more significant discrepancy. This comparison demonstrates that the current, more complete model is an important improvement from the previous ones.

2.5 Conclusions

In conclusion, we have systematically analyzed the stability of electrified and stratified fluids using the Taylor-Melcher leaky dielectric model. The transfer relations developed by Melcher are universally applicable to this (and many other) class of problems, and can be used to obtain analytical dispersion relations in a straightforward manner. Both new results and those from previous work are derived as special cases of the general solutions presented. Although we only consider a normal applied field in the limit of instantaneous relaxation, other problems such as those with a parallel applied field and a finite relaxation time can be treated similarly. In addition, this approach can also be potentially applied to different geometric configurations, e.g. to a cylindrical geometry with axisymmetry. However, for this case the transfer relations need to be derived first by solving equations (A.1-A.5) in the corresponding coordinate system.

Chapter 3

A Transient Analysis for Droplet Electrodeformations

3.1 Introduction

In this chapter, we develop a transient analysis for droplet electrodeformations. The droplet interface separates two fluids phases with arbitrary properties including viscosity, conductivity, and permittivity. The droplet is assumed to be spheroidal in shape with volume conservation. The Taylor-Melcher leaky dielectric model is adopted, where the electrical and the hydrodynamic problem can be solved separately, and then coupled at the interface with stress matching conditions. We first consider the general situation of a finite relaxation time. In this framework, instantaneous charge relaxation is treated as a special limiting case. The equations are recast into a rotational spheroidal coordinate system, and reduced to the single ODE governing the change of the aspect ratio as a function of time. The model is extensively validated by comparing predicted deformation with both previous theoretical and numerical studies, and with experimental data. This work is a necessary building block for the more complex task in the next chapter, namely, the development of a vesicle electrodeformation model. This work has been summarized in a manuscript submitted to Journal of Fluid Mechanics [89].

3.2 Theory

A schematic of the problem configuration is shown in figure 3.1(a). An uncharged, neutrally buoyant liquid droplet of radius r_0 is suspended in another fluid, and is subject to an applied electric field of strength E_0. We assume that the fluids are immiscible leaky dielectrics with constant electrical and mechanical properties. σ, ϵ, and μ are the electrical conductivity, permittivity, and fluid viscosity, and the subscripts i and e

denote internal and external, respectively. Under the influence of an applied electric field, free charges accumulate at the interface, which induces droplet deformation and EHD flows both inside and outside the droplet. Taylor [74] predicted that droplets may deform into prolate or oblate shapes depending on the electrical properties of the fluids. In the following analysis, we focus on developing a solution for prolate deformations, whereas a solution for oblate deformations can be pursued in a similar manner (not presented here).

We assume that the droplet remains spheroidal in shape throughout the process. This approximation is consistent with experimental observations in [24] and [7]. Following Taylor [73], Bentenities and Krause [7], and Dubashe and Mestel [16], the natural coordinate system to analyze this problem is the prolate spheroidal coordinate system, and a schematic is shown in figure 3.1(b). The geometry is assumed to be axisymmetric about the z axis, which aligns with the direction of the applied electric field. The spheroidal coordinates $(\xi,\ \eta)$ are related to the cylindrical coordinates $(r,\ z)$ through the equations:

$$z = c\xi\eta, \tag{3.1}$$

$$r = c\sqrt{(\xi^2-1)(1-\eta^2)}. \tag{3.2}$$

Here $c = \sqrt{a^2-b^2}$ is chosen to be the semi-focal length of the spheroidal droplet, and a and b are the major and minor semi-axis, respectively. The contours for constant ξ are spheroids, and $\xi \in [1,\ +\infty)$. The contours for constant η are hyperboloids, and $\eta \in [-1,\ 1]$. The surface of the prolate spheroid is conveniently given as

$$\xi = \xi_0 \equiv \frac{a}{c}. \tag{3.3}$$

For the derivation below, we further assume that the volume of the droplet is conserved. We subsequently obtain

$$a = r_0(1-\xi_0^{-2})^{-\frac{1}{3}}, \qquad b = r_0(1-\xi_0^{-2})^{\frac{1}{6}}. \tag{3.4}$$

Therefore, the droplet geometry is completely characterized by a single parameter, ξ_0,

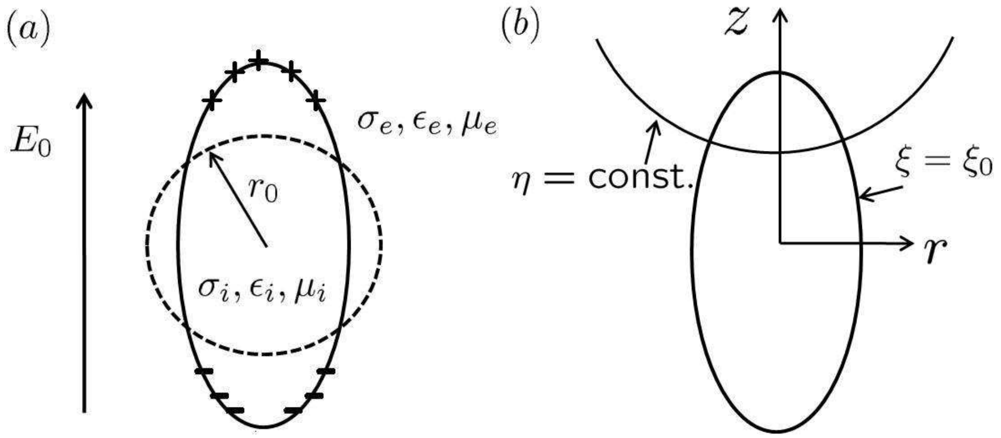

Figure 3.1: (a) A schematic of the problem configuration. (b) The prolate spheroidal coordinate system.

which evolves in time along with deformation. The critical idea of the current analysis is to express all variables, e.g. the electric potential and the stream function in terms of ξ_0.

In what follows, we will solve the electrical problem first, followed by a solution of the hydrodynamic problem. An ODE for ξ_0 is obtained by applying both the stress matching and kinematic conditions.

3.2.1 The electrical problem

The electric potentials inside and outside the droplet obey the Laplace equation according to the Ohmic law of current conservation with uniform electrical conductivity:

$$\nabla^2\phi_i = \nabla^2\phi_e = 0. \tag{3.5}$$

The matching conditions at the interface are

$$||\nabla\phi \cdot \boldsymbol{t}|| = 0, \qquad \text{at } \xi = \xi_0, \tag{3.6}$$

$$\frac{\partial q}{\partial t} - ||\sigma\nabla\phi \cdot \boldsymbol{n}|| = 0, \qquad \text{at } \xi = \xi_0. \tag{3.7}$$

Here $||\cdot||$ denotes a jump across an interface, and $\boldsymbol{t}$ and $\boldsymbol{n}$ are the unit tangential and normal interfacial vector, respectively. $q = || -\epsilon\nabla\phi\cdot\boldsymbol{n}||$ is the surface charge density. Note that in equation (3.7), we have included the displacement current, $\partial q/\partial t$. This term is particularly important for fluids with very low conductivities (for example, those used in [24]) such that the interfacial charging time becomes comparable to the deformation time. However, we have ignored the effect of surface charge convection which is shown to be small by numerical simulations [19]. Equation (3.7) can be rewritten in terms of the electric potentials,

$$\begin{aligned}(\frac{\epsilon_e}{c}\frac{\partial\phi_e}{\partial\xi} &- \frac{\epsilon_i}{c}\frac{\partial\phi_i}{\partial\xi})\frac{d\frac{c}{h_\xi}}{dt} - (\frac{\epsilon_e}{h_\xi c}\frac{\partial\phi_e}{\partial\xi} - \frac{\epsilon_i}{h_\xi c}\frac{\partial\phi_i}{\partial\xi})\frac{dc}{dt} \\ &+ (\frac{\epsilon_e}{h_\xi}\frac{\partial^2\phi_e}{\partial\xi\partial t} - \frac{\epsilon_i}{h_\xi}\frac{\partial^2\phi_i}{\partial\xi\partial t}) + \frac{1}{h_\xi}(\sigma_e\frac{\partial\phi_e}{\partial\xi} - \sigma_i\frac{\partial\phi_i}{\partial\xi}) = 0, \qquad \text{at } \xi = \xi_0. \quad (3.8)\end{aligned}$$

Here h_ξ is a metric coefficient of the prolate spheroidal coordinate system. The displacement current consists of two parts, represented by the first three terms on the LHS of the above equation. The first two terms result from a change in the droplet shape, and the third results from the charging process as if the shape remains unchanged. Here, we assume that the first term is negligible compared with the other two, and equation (3.8) can be further simplified to be

$$\epsilon_e\frac{\partial^2\phi_e}{\partial\xi\partial t} - \frac{\epsilon_e}{c}\frac{\partial\phi_e}{\partial\xi}\frac{dc}{dt} - \epsilon_i\frac{\partial^2\phi_i}{\partial\xi\partial t} + \frac{\epsilon_i}{c}\frac{\partial\phi_i}{\partial\xi}\frac{dc}{dt} + \sigma_e\frac{\partial\phi_e}{\partial\xi} - \sigma_i\frac{\partial\phi_i}{\partial\xi} = 0, \qquad \text{at } \xi = \xi_0. \quad (3.9)$$

Indeed a consistency check *a posteriori* justifies the simplification. Far away from the droplet surface the electric field is uniform,

$$-\nabla\phi_e = E_0\boldsymbol{z}, \qquad \text{at } \xi \to \infty. \quad (3.10)$$

We also require that ϕ_i remains finite at $\xi = 1$. For the initial condition, we assume both the electric potential and the normal component of the displacement vector are continuous:

$$\epsilon_e\frac{\partial\phi_e}{\partial\xi} = \epsilon_i\frac{\partial\phi_i}{\partial\xi}, \quad \phi_e = \phi_i, \qquad \text{at } \xi = \xi_0,\ t = 0. \quad (3.11)$$

Solutions for the electric potentials have been obtained previously without including the displacement current [7, 74]. With its inclusion the approach is similar and the results are

$$\phi_e = E_0 r_0 \left[-\lambda\xi + \alpha Q_1(\xi)\right]\eta, \tag{3.12}$$

$$\phi_i = E_0 r_0 \beta \xi \eta. \tag{3.13}$$

Here, $Q_1(\xi)$ is a 1st-degree Legendre polynomial of the second kind. $\lambda \equiv c/r_0$ is the dimensionless semi-focal length. The coefficients α and β are determined by the interfacial matching conditions (3.6) and (3.9) which gives

$$\alpha = \frac{\beta\xi_0 + \lambda\xi_0}{Q_1(\xi_0)}, \tag{3.14}$$

$$\begin{aligned} \frac{\tau_1}{\tau_2}\left[\frac{Q_1^{'}(\xi_0)\xi_0}{Q_1(\xi_0)} - \frac{1}{\epsilon_r}\right]\frac{d\beta}{d\tau} + \left[\frac{\tau_1}{\tau_2}\left(\frac{Q_1^{'}(\xi_0)}{Q_1(\xi_0)} + \frac{Q_1^{''}(\xi_0)Q_1(\xi_0) - Q_1^{'2}(\xi_0)}{Q_1^2(\xi_0)}\xi_0\right)\frac{d\xi_0}{d\tau}\right. \\ \left. -\frac{\tau_1}{\tau_2}\left(\frac{Q_1^{'}(\xi_0)\xi_0}{Q_1(\xi_0)\lambda} - \frac{1}{\epsilon_r\lambda}\right)\frac{d\lambda}{d\xi_0}\frac{d\xi_0}{d\tau} + \frac{Q_1^{'}(\xi_0)\xi_0}{Q_1(\xi_0)} - \frac{1}{\sigma_r}\right]\beta + \lambda\left[\frac{Q_1^{'}(\xi_0)\xi_0}{Q_1(\xi_0)} - 1\right] \\ +\frac{\tau_1}{\tau_2}\left[\frac{Q_1^{'}(\xi_0)}{Q_1(\xi_0)} + \frac{Q_1^{''}(\xi_0)Q_1(\xi_0) - Q_1^{'2}(\xi_0)}{Q_1^2(\xi_0)}\xi_0\right]\lambda\frac{d\xi_0}{d\tau} = 0, \end{aligned} \tag{3.15}$$

$$\alpha(0) = \lambda\xi_0\left(\epsilon_r - 1\right), \qquad \beta(0) = \frac{\epsilon_r\lambda\left(Q_1(\xi_0) - Q_1^{'}(\xi_0)\xi_0\right)}{\epsilon_r Q_1^{'}(\xi_0)\xi_0 - Q_1(\xi_0)}. \tag{3.16}$$

Here $\epsilon_r \equiv \epsilon_e/\epsilon_i$ and $\sigma_r \equiv \sigma_e/\sigma_i$ are the permittivity ratio and the conductivity ratio, respectively. $\tau_1 \equiv \epsilon_e/\sigma_e$ is an electrical charging time. $\tau_2 \equiv r_0\mu_e/\gamma$ is a characteristic flow timescale used below in the hydrodynamic problem, and γ is the coefficient of surface tension. In the above equations, a dimensionless time $\tau \equiv t/\tau_2$ has been used. In general, equation (3.15) needs to be integrated together with an ODE for ξ_0 to obtain α and β. However, in the limit of instantaneous-charge-relaxation time, $\tau_1/\tau_2 \to 0$, and equation (3.15) can be simplified to be

$$\left[\frac{Q_1^{'}(\xi_0)\xi_0}{Q_1(\xi_0)} - \frac{1}{\sigma_r}\right]\beta + \lambda\left[\frac{Q_1^{'}(\xi_0)\xi_0}{Q_1(\xi_0)} - 1\right] = 0. \tag{3.17}$$

This result is equivalent to a solution employing the simplified boundary condition $||\sigma \nabla \phi \cdot \boldsymbol{n}|| = 0$ in place of equation (3.7).

The normal and tangential electrostatic stresses are given by,

$$S_{\xi\xi} = \frac{\epsilon}{2}\left(E_\xi^2 - E_\eta^2\right), \qquad S_{\xi\eta} = \epsilon E_\xi E_\eta, \tag{3.18}$$

where $E_\xi = -(\partial\phi/\partial\xi)/h_\xi$ and $E_\eta = -(\partial\phi/\partial\eta)/h_\eta$ are the normal and tangential electric fields, respectively. h_η is a metric coefficient of the prolate spheroidal coordinate system. These stresses can be evaluated with the solutions (3.12) and (3.13), and will be used in the stress matching conditions below.

3.2.2 The hydrodynamic problem

In the regime of low-Reynolds-number flow, the governing equation for the hydrodynamic problem can be rewritten in terms of the stream function, ψ, as

$$\nabla^4 \psi = 0. \tag{3.19}$$

Here, the stream function is related to the velocity components as

$$u = -\frac{1}{h_\xi h_\theta}\frac{\partial \psi}{\partial \xi}, \qquad v = \frac{1}{h_\eta h_\theta}\frac{\partial \psi}{\partial \eta}. \tag{3.20}$$

h_θ is a metric coefficient of the prolate spheroidal coordinate system. At the interface, u and v represent the tangential and normal velocities, respectively, and they are required to be continuous

$$u_e = u_i, \qquad v_e = v_i, \qquad \text{at } \xi = \xi_0. \tag{3.21}$$

In addition, we prescribe a kinematic condition relating the interfacial displacement to the normal velocity,

$$v(\xi = \xi_0,\, \eta) = \frac{r_0\left(1-\xi_0^{-2}\right)^{-5/6}}{3\xi_0^2}\frac{\left(1-3\eta^2\right)}{\sqrt{\xi_0^2-\eta^2}}\frac{d\xi_0}{dt}. \tag{3.22}$$

The total force on the interface resulting from the electrical stress, the hydrodynamic stress, and the surface tension should be balanced at every point. However, this constraint is impossible to satisfy exactly within the framework of spheroidal deformation. Various authors developed reduced stress-balance conditions instead [7, 16, 70, 73]. Here we follow the integrated formulae proposed by Sherwood [70] and Dubash and Mestel [16]

$$\int u \cdot \left(T^e_{\xi\eta} - T^i_{\xi\eta} + S^e_{\xi\eta} - S^i_{\xi\eta}\right) ds = 0, \tag{3.23}$$

$$\int v \cdot \left(T^e_{\xi\xi} - T^i_{\xi\xi} + S^e_{\xi\xi} - S^i_{\xi\xi} - \gamma\left(\frac{1}{R_1} + \frac{1}{R_2}\right)\right) ds = 0. \tag{3.24}$$

Equations (3.23) and (3.24) represent a global balance of the tangential and normal stresses, respectively derived from energy principles. Here T denotes the hydrodynamic stress, R_1 and R_2 are the two principal radii of the curvature, and the integration is carried over the interface.

The general solution to (3.19) was proposed by Dassios *et al.* [13] using the method of semi-separation:

$$\psi = g_0(\xi)G_0(\eta) + g_1(\xi)G_1(\eta) + \sum_{n=2}^{\infty}\left[g_n(\xi)G_n(\eta) + h_n(\xi)H_n(\eta)\right]. \tag{3.25}$$

Here G_n and H_n are Gegenbauer functions of the first and second kind, respectively. g_n and h_n are linear combinations of G_n and H_n. The detailed expressions for G_n, H_n, g_n, and h_n are found in [13]. Interested readers are referred to [13] for further details. After considering that the far field is quiescent, and that the velocities remain finite at $\xi = 1$, the stream functions can be simplified to be

$$\psi_e = \sum_{n=1}^{\infty}\left[A^{2n-1}_{2n+1}H_{2n-1}(\xi) + A^{2n+1}_{2n+1}H_{2n+1}(\xi) + A^{2n+3}_{2n+1}H_{2n+3}(\xi)\right]G_{2n+1}(\eta), \tag{3.26}$$

$$\psi_i = \sum_{n=1}^{\infty}\left[B^{2n-1}_{2n+1}G_{2n-1}(\xi) + B^{2n+1}_{2n+1}G_{2n+1}(\xi) + B^{2n+3}_{2n+1}G_{2n+3}(\xi)\right]G_{2n+1}(\eta), \tag{3.27}$$

where A and B are unknown coefficients satisfying the relations $A^{2n+3}_{2n+1} = A^{2n+1}_{2n+3}$, $B^{2n+3}_{2n+1} = B^{2n+1}_{2n+3}$. In general, these coefficients are inter-dependent, and the full solution can be obtained only with the entire infinite series. Here we seek a truncated solution as an approximation,

$$\psi_e = \left[A_3^1 H_1(\xi) + A_3^3 H_3(\xi)\right] G_3(\eta), \tag{3.28}$$

$$\psi_i = \left[B_3^3 G_3(\xi) + B_3^5 G_5(\xi)\right] G_3(\eta). \tag{3.29}$$

Indeed, $G_3(\eta)$ gives a functional form in η confirming with that in equation (3.22), which can be rewritten as

$$v(\xi = \xi_0,\, \eta) = \frac{2c^2\sqrt{\xi_0 - 1} r_0 \left(1 - \xi_0^{-2}\right)^{-5/6}}{3\xi_0^2} \frac{G_3'(\eta)}{h_\eta h_\theta} \frac{d\xi_0}{dt}. \tag{3.30}$$

This agreement in part validates the spheroidal shape assumption: the shape represents the leading mode in the infinite series.

Equations (3.21-3.24) are combined to solve for the five unknown variables, namely, A_3^1, A_3^3, B_3^3, B_3^5, and ξ_0. Specifically, equations (3.21) and (3.22) are first used to eliminate the A_3^1, B_3^3, B_3^5,

$$A_3^1 = H_3(\xi_0) A_3^3 - M\frac{d\xi_0}{dt}, \tag{3.31}$$

$$B_3^3 = \frac{-G_5(\xi_0)H_3'(\xi_0)A_3^3 + G_5'(\xi_0)M\frac{d\xi_0}{dt}}{N}, \tag{3.32}$$

$$B_3^5 = \frac{G_3(\xi_0)H_3'(\xi_0)A_3^3 - G_3'(\xi_0)M\frac{d\xi_0}{dt}}{N}, \tag{3.33}$$

where $M \equiv 2r_0^3/3(\xi_0^3 - \xi_0)$, and $N \equiv G_3(\xi_0)G_5'(\xi_0) - G_3'(\xi_0)G_5(\xi_0)$. Further considering equation (3.23), we can express A_3^3 in terms of ξ_0,

$$A_3^3 = \frac{\begin{array}{r} c r_0^2 \epsilon_i E_0^2 \left\{\xi_0\beta^2 - \epsilon_r(\lambda - \alpha Q_1'(\xi_0))(\lambda\xi_0 - \alpha Q_1(\xi_0))\right\} f_{11}(\xi_0) \\ -\mu_i\left\{(\mu_r - 1) f_{12}(\xi_0) + f_{13}(\xi_0)\right\} M\frac{d\xi_0}{dt} \end{array}}{-\mu_i\left\{\mu_r f_{14}(\xi_0) + f_{15}(\xi_0)\right\}}, \tag{3.34}$$

where $\mu_r \equiv \mu_e/\mu_i$ is the viscosity ratio. The detailed expressions of $f_{11}(\xi_0) - f_{15}(\xi_0)$ are found in the Appendix C. This expression is inserted into equation (3.24) to obtain the final result, an ODE governing the evolution of the ξ_0,

$$\frac{d\xi_0}{d\tau} = -\frac{1}{F}\left[Q_N f_{21}(\xi_0) + Q_T \frac{\mu_r f_{22}(\xi_0) + f_{23}(\xi_0)}{\mu_r f_{14}(\xi_0) + f_{15}(\xi_0)} - f_{24}(\xi_0)\right], \tag{3.35a}$$

$$Q_N = \frac{Ca_E}{\lambda^2}\left[(\lambda - \alpha Q_1'(\xi_0))^2 + (\lambda - \alpha Q_1(\xi_0)/\xi_0)^2 - 2\beta^2/\epsilon_r\right], \tag{3.35b}$$

$$Q_T = \frac{Ca_E}{\lambda^2}\left[(\lambda - \alpha Q_1'(\xi_0))(\lambda - \alpha Q_1(\xi_0)/\xi_0) - \beta^2/\epsilon_r\right]. \tag{3.35c}$$

The detailed expressions of $f_{21}(\xi_0) - f_{24}(\xi_0)$, and F are also found in the Appendix C. The coefficients α and β are given by equations (3.14) and (3.15), respectively. $Ca_E \equiv r_0\epsilon_e E_0^2/\gamma$ is the electric capillary number. In equation (3.35a), the three terms in the numerator on the RHS represent the contributions from the normal stress, the tangential stress, and the surface tension, respectively. At the equilibrium, the balance of the three forces determines the final shape. The leading coefficients Q_N and Q_T arise exclusively from the electrostatic stresses, and can be used to estimate their respective influence on deformation. In the limit of instantaneous relaxation, and by considering equations (3.14) and (3.17), Q_N and Q_T can be simplified to be

$$Q_N = Ca_E K^2(\sigma_r^2 + 1 - 2\sigma_r^2/\epsilon_r), \quad Q_T = Ca_E K^2 \sigma_r(1 - \sigma_r/\epsilon_r), \tag{3.36}$$

$$K \equiv \frac{Q_1(\xi_0) - \xi_0 Q_1'(\xi_0)}{Q_1(\xi_0) - \sigma_r \xi_0 Q_1'(\xi_0)}. \tag{3.37}$$

For this case, the evolution of ξ_0 is governed by a single timescale, τ_2. Once ξ_0 is obtained by solving the equations (3.15) and (3.35a), the aspect ratio is calculated by the formula

$$\frac{a}{b} = (1 - \xi_0^{-2})^{-\frac{1}{2}}. \tag{3.38}$$

3.3 Comparison with previous results

In this section, we compare our model prediction extensively with results from previous work. The comparisons with theoretical/numerical results and experimental data are respectively presented in §3.3.1 and §3.3.2.

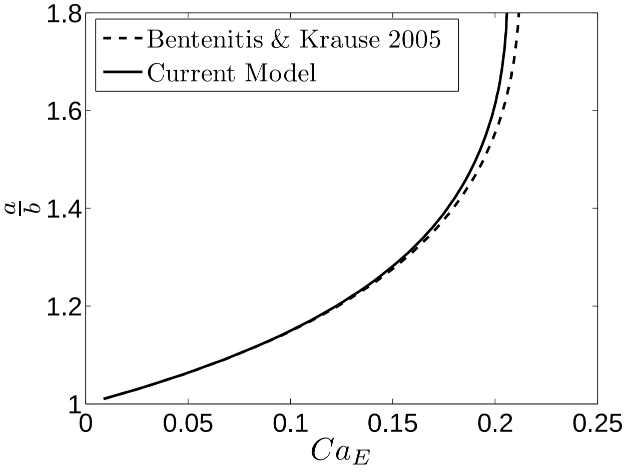

Figure 3.2: The equilibrium aspect ratio as a function of electric capillary number. The parameters are $\sigma_r = 1.19 \times 10^{-2}$, $\epsilon_r = 3.24 \times 10^{-1}$, and $\mu_r = 7.33 \times 10^{-2}$.

3.3.1 Comparison with previous theories and simulation

We first consider the equilibrium shape, and compare our results with those from Bentenitis and Krause [7]. For this case, the LHS of equation (3.35a) is simply set to zero, resulting in the so called discriminating equation,

$$Q_N f_{21}(\xi_0) + Q_T \frac{\mu_r f_{22}(\xi_0) + f_{23}(\xi_0)}{\mu_r f_{14}(\xi_0) + f_{15}(\xi_0)} = f_{24}(\xi_0). \tag{3.39}$$

Here Q_N and Q_T are given by equation (3.36). ξ_0 is solved as a root(s) of this equation from which the equilibrium aspect ratio, a/b, can be obtained. Equation (3.39) shows that the equilibrium shape is only determined by the dimensionless parameters Ca_E, σ_r, ϵ_r, and μ_r. A comparison with the theoretical prediction by Bentenitis and Krause [7] is shown in figure 3.2. Note that in this earlier work, the authors solved for the equilibrium shape directly without obtaining the transient solution. A good agreement is observed, although a different stress matching condition has been used by Bentenitis and Krause [7] (see equations (38) and (45) therein).

We next compare with the results from Dubash and Mestel [16]. In this work, the authors developed a theoretical model, also with the spheroidal shape assumption, to predict the transient deformation of a conducting, inviscid droplet immersed in a

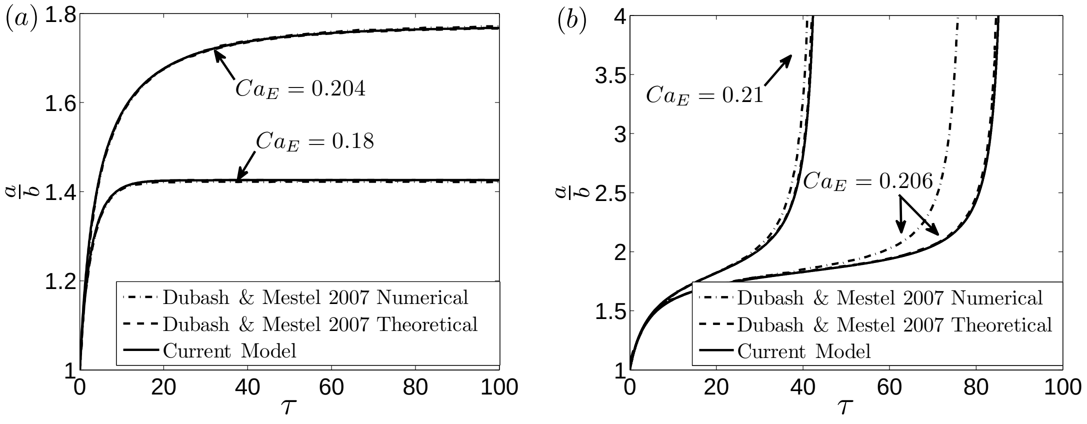

Figure 3.3: The deformation of a conducting droplet in a highly viscous medium. (a) $Ca_E = 0.18$ and 0.204. (b) $Ca_E = 0.206$ and 0.21. The dimensionless time τ is defined as $\tau = t/\tau_2$, where $\tau_2 = r_0\mu_e/\gamma$.

viscous, nonconductive solution. This special consideration leads to significant simplifications: both the electric and hydrodynamic fields are absent within the droplet. In addition, at the equilibrium state (if one is permitted), the hydrodynamic flow outside the droplet is also quiescent, giving rise to the phenomenon termed EHS.

In our generalized framework, the solution for this case is simply achieved by setting $\sigma_r \to 0$ and $\mu_r \to \infty$ in equations (3.35a) and (3.36). Note that $\sigma_r \to 0$ directly leads to instantaneous charge relaxation. The resulting comparisons are shown in figure 3.3 in which the aspect ratio (a/b) is plotted as a function of time for four different electric capillary numbers (Ca_E). For the two lower values of Ca_E, the current model has excellent agreement with both the theoretical and numerical predictions by Dubash and Mestel [16] (figure 3.3a). For these Ca_E values, final equilibria are achieved. As Ca_E increases (figure 3.3b), the deformation becomes unstable and an equilibrium shape is no longer possible. The rapid expansion with a sharp slope at the later stage preludes droplet breakup. For these two cases, the theoretical models still agree with each other, whereas some discrepancies exist with respect to the numerical simulation, in particular for Ca_E=0.206. However, this discrepancy is in general only noticeable when the Ca_E number is above and very close to the critical threshold of breakup (Ca_E ~0.2044 for the case studied), due to a slight underprediction of the rate of deformation by the theoretical models. A similar trend is observed when comparing with the numerical simulation by Hirata *et al.* [26] (not shown). Overall, our model can serve as a good approximation to the numerical model which is considered more accurate.

3.3.2 Comparison with experimental data

The main source of experimental data comes from Ha and Yang [24]. We also begin with an examination of the final aspect ratio when an equilibrium shape can be achieved. Figure 3.4 shows the equilibrium aspect ratio of a castor oil droplet immersed in silicone oil from Ha and Yang [24], as well as predicted by various models. The current prediction is shown as a solid line, whereas the results from first-order [74] and second-order [1] theories are shown as dot-dashed and dashed lines, respectively. Following Lac and Homsy [37], we rescale Ca_E to best match Ajayi's second-order correction. This rescaling is equivalent to adjusting the surface tension from $\gamma = 3.3 \times 10^{-3}$ N/m used by Ha and Yang [24] (which is a fitting parameter in that work) to $\gamma = 4.3 \times 10^{-3}$ N/m. The latter value is close to the lower bound, $\gamma = 4.5 \times 10^{-3}$ N/m, measured by Salipante and Vlahovska [65]. In addition, we use $\sigma_r = 0.03$ according to the measurements by Torza *et al.* [77], Vizika and Saville [80], and Salipante and Vlahovska [65], which is slightly different from the value of $\sigma_r = 0.04$ used by Lac and Homsy [37]. The results show good agreement between the current model and the experimental data. Most importantly, our theory correctly predicts a critical Ca_E ($\sim$0.244) for droplet breakup. In contrast, the small deformation theories can not capture this critical phenomenon.

We have also compared our theoretical prediction with the experimental data from Bentenitis and Krause [7], which measured the equilibrium aspect ratio of a DGEBA droplet immersed in a PDMS solution. Since our result is in good agreement with the theoretical prediction in the same work (see figure 3.2), which in turn agrees well with the data, the comparison is not shown here for brevity.

Next, we will compare the transient solution from our model with data from Ha and Yang [24]. In figure 3.5(a), the data is extracted from figure 3 in the latter work, which captures the deformation of a water droplet in silicone oil. The droplet is fitted with an ellipse at every instant, based on which the aspect ratio is calculated. A 10% fitting

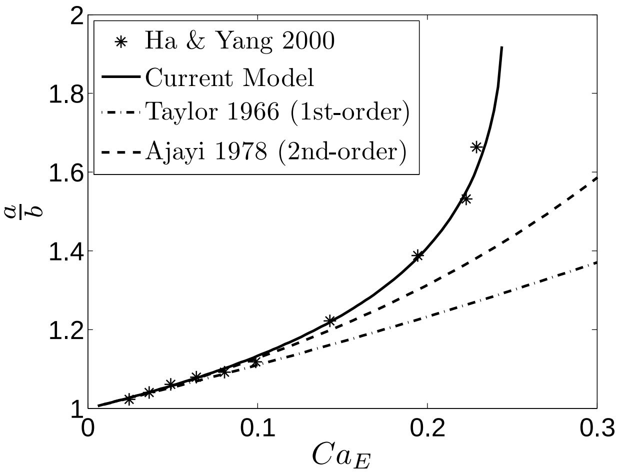

Figure 3.4: The prediction from current model is compared with the small deformation theories [1, 74] and experimental data [24]. The parameters are $\sigma_r = 0.03$, $\epsilon_r = 0.73$, and $\mu_r = 1.14$.

error is estimated, and is shown as error bars in figure 3.5(a) (the same approach is adopted to extract the data presented in figures 3.5b and 3.6). The model prediction is calculated with equations (3.35a) and (3.36), and with $\sigma_r = 1 \times 10^{-6}$, $\epsilon_r = 3.55 \times 10^{-2}$, $\mu_r = 1000$, $E_0 = 3.2$ kV/cm, $r_0 = 0.25$ cm, and $\mu_e = 0.98$ Pa $\cdot$ s all directly taken from Ha and Yang [24]. For medium permittivity, we use $\epsilon_e = 2.478 \times 10^{-11}$ F/m following the measurements by Torza *et al.* [77], Vizika and Saville [80], and Salipante and Vlahovska [65]. For surface tension, we use $\gamma = 3.037 \times 10^{-2}$ N/m, which is consistent with the values reported by Torza *et al.* [77] and Vizika and Saville [80]. In this case, the model is able to predict the deformation process with good quantitative accuracy. In figure 3.5(b), a similar comparison is shown for a water-ethanol droplet in silicone oil. The data is based on figure 4 in [24]. For our calculation, $\sigma_r = 1 \times 10^{-5}$, $\epsilon_r = 0.05$, $\mu_r = 23.3$, $E_0 = 4.5$ kV/cm, $r_0 = 0.14$ cm, $\mu_e = 0.98$ Pa $\cdot$ s, and $\epsilon_e = 2.478 \times 10^{-11}$ F/m. Because the droplet is doped with polyvinylpyrrolidone (a polymer solution), the surface tension is not directly available, and is used as a fitting parameter instead to generate the best agreement between theory and data. The resulting value is $\gamma = 3.432 \times 10^{-2}$ N/m, 11% higher than that for water/silicone oil which is used in figure 3.5(a).

In contrast to the regime of instantaneous charge relaxation examined in figure 3.5,

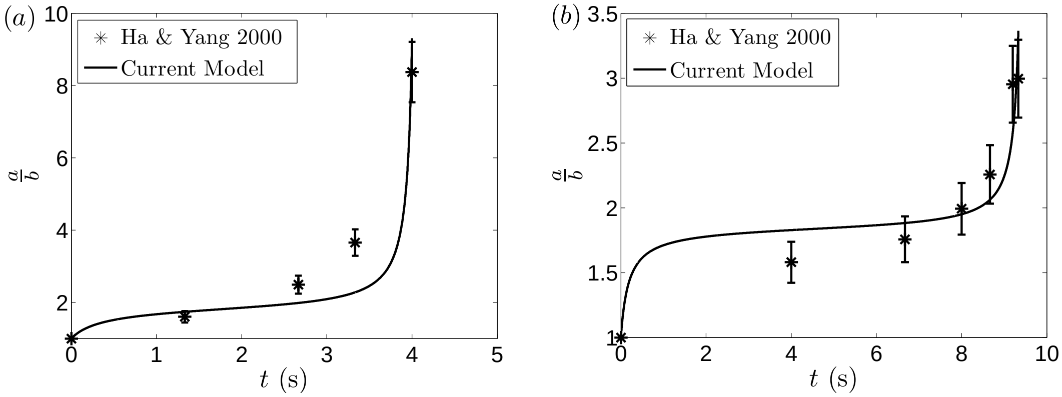

Figure 3.5: Comparison of transient droplet deformation. (a) A water droplet in silicone oil. The parameters are $\sigma_r = 1 \times 10^{-6}$, $\epsilon_r = 3.55 \times 10^{-2}$, $\mu_r = 1000$, $E_0 = 3.2$ kV/cm, $r_0 = 0.25$ cm, $\mu_e = 0.98$ Pa · s, $\epsilon_e = 2.478 \times 10^{-11}$ F/m, and $\gamma = 3.037 \times 10^{-2}$ N/m. (b) A water-ethanol droplet in silicone oil. The parameters are $\sigma_r = 1 \times 10^{-5}$, $\epsilon_r = 0.05$, $\mu_r = 23.3$, $E_0 = 4.5$ kV/cm, $r_0 = 0.14$ cm, $\mu_e = 0.98$ Pa · s, $\epsilon_e = 2.478 \times 10^{-11}$ F/m, and $\gamma = 3.432 \times 10^{-2}$ N/m.

figure 3.6 represents droplet deformation in the finite-charging-time regime. The data is extracted from figure 7 in [24]. For this case, the droplet is made of castor oil, and is immersed in silicone oil. The extremely low conductivities of these media lead to a charging time (∼seconds) comparable to the deformation time, and the full model, equations (3.35a-3.35c), has to be used. For our calculation, $\sigma_r = 0.03$, $\epsilon_r = 0.73$, $\mu_r = 1.14$, $E_0 = 3.2$ kV/cm, $r_0 = 0.16$ cm, $\mu_e = 0.9$ Pa · s, $\epsilon_e = 2.478 \times 10^{-11}$ F/m, and $\gamma = 5 \times 10^{-3}$ N/m. Note that the values for the surface tension and the conductivity ratio follow the measurements by Torza *et al.* [77], Vizika and Saville [80], and Salipante and Vlahovska [65] which are believed to be more accurate than the original values of $\sigma_r = 0.1$ and $\gamma = 3.3 \times 10^{-3}$ N/m given by Ha and Yang [24]. In addition, the actual conductivity of silicone oil varies from 10^{-10} S/m to 10^{-13} S/m in the literature [33, 58, 65]. In figure 3.6, we show the calculation with three representative values within this range, namely, $\sigma_e = 1 \times 10^{-10}$, 7×10^{-12}, and 1×10^{-12} S/m. The best agreement is found for $\sigma_e = 7 \times 10^{-12}$ S/m. For comparison, the calculation according to the instantaneous-charge-relaxation model (equations (3.35a) and (3.36)) is also shown, and is denoted by ICR. This simplified model clearly overpredicts deformation by a significant degree.

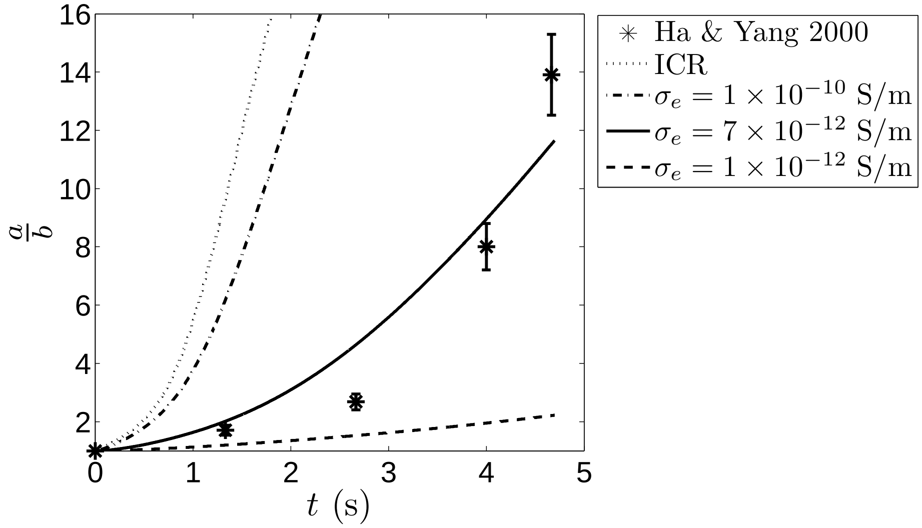

Figure 3.6: Droplet deformation in the limit of extremely low conductivities. The parameters are $\sigma_r = 0.03$, $\epsilon_r = 0.73$, $\mu_r = 1.14$, $E_0 = 3.2$ kV/cm, $r_0 = 0.16$ cm, $\mu_e = 0.9$ Pa $\cdot$ s, $\epsilon_e = 2.478 \times 10^{-11}$ F/m, and $\gamma = 5 \times 10^{-3}$ N/m. The best agreement between the data and the theory is found for $\sigma_e = 7 \times 10^{-12}$ S/m. For reference, the dotted line shows the calculation according to the instantaneous-charge-relaxation (ICR) model.

In general, our model agrees well with experimental data in both steady and transient states, and for a large parametric range. These comparisons provide a strong validation for our model.

3.4 The effects of stresses on deformation

In this section, we demonstrate the utility of our theoretical results by analyzing in-depth the governing equation. For simplicity, we focus on the regime of instantaneous relaxation, where Q_N and Q_T are given by equation (3.36). A main contribution of the current work is that equation (3.35a) clearly separates the effects by different forces. In the numerator of the RHS, the three terms represent respectively the effects of the normal stresses (both electrical and hydrodynamic), the tangential stresses (both electrical and hydrodynamic), and the surface tension. Furthermore, all the functions in this equation are positive (f_{14}, f_{15}, $f_{21} - f_{24}$, F), such that the signs of Q_N and Q_T completely determine whether the normal and tangential stresses would promote or suppress deformation. Due to the inverse relationship between ξ_0 and the aspect ratio, a/b (see equation (3.38)), a positive Q_N or Q_T indicates a positive contribution. Evidently, surface tension always resists deformation. Because Q_N and Q_T depend exclusively on the electrical properties in a simple manner (see equation (3.36)), their influences can be conveniently analyzed using a phase diagram shown in figure 3.7. The dashed and dotted lines correspond to $Q_N = 0$ and $Q_T = 0$, respectively. These lines separate the phase space into three regimes, where N and T denote the normal and tangential stresses, and the superscripts $'+'$ and $'-'$ denote a positive or negative contribution to deformation, respectively. In addition, the solid line is obtained by solving for the root of Taylor's discriminating function [74], which separates the prolate (denoted by $'Pr'$) and oblate (denoted by $'Ob'$) regimes (this line can be equivalently obtained by looking for the steady-state solution of $a/b = 1$ from equation (3.39)).

Figure 3.7 can be used to shed light on the physical processes governing deformation. First, the line for $Q_T = 0$ separates the T^+ and T^- regimes, which corroborates with the previous results [37, 74]. On this dividing line, the velocity field becomes zero, so does the tangential electrical stress. In [37], the viscosity ratio has opposite effects on deformation in the T^+ and T^- regimes. This behavior is clearly explained by equation (3.35a). Second, there is a small region within the oblate regime, namely, the area between the solid and dashed lines where Q_N is positive. This suggests that the normal stress still tends to stretch the droplet along the direction of the applied field. However, because Q_T is negative, the tangential stresses overcome the normal stresses, and stretch the droplet into an oblate shape. This new insight is not available from previous analysis or simulations.

Third, in the prolate regime where Q_N is always positive, the sign of Q_T leads to different deformation behavior. Figure 3.8 shows the equilibrium aspect ratio as a function of Ca_E for three specific cases. Note that the new variable

$$D = \frac{a-b}{a+b}. \tag{3.40}$$

In this new definition, $D = 0$ corresponds to $a/b = 1$, and $D = 1$ corresponds to

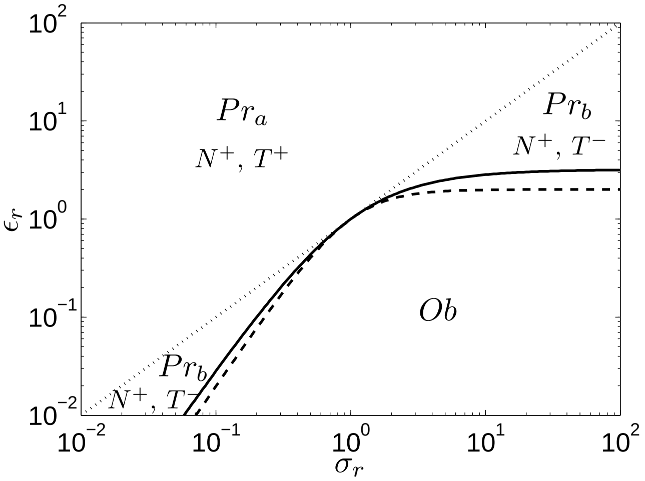

Figure 3.7: Phase diagram for droplet deformation. Here the dotted line is calculated by satisfying $Q_T = 0$. The solid line is calculated by solving for the root of Taylor's discriminating function. The dashed line represents $Q_N = 0$. Pr and Ob denote prolate and oblate deformation, respectively. N and T denote the effect of normal and tangential stresses, respectively, and a $'+'$ or $'-'$ sign denotes facilitating or suppressing, respectively.

$a/b \to \infty$. For all three cases, $\epsilon_r = 10$ and $\mu_r = 1$. For $\sigma_r = 0.05$, $Q_T > 0$. We observe hysteresis, and D approaches 1 rapidly in the upper brunch. The cases of $\sigma_r = 1$ and $\sigma_r = 30$ correspond to $Q_T = 0$ and $Q_T < 0$, respectively. In general, as Q_T decreases, the deformation becomes weaker for comparable Ca_E values. Most interestingly, for $\sigma_r = 30$ ($Q_T < 0$), D converges to a value less than 1 in the limit of $Ca_E \to \infty$. This means that even for the very large applied electric field strength, a finite equilibrium aspect ratio can be achieved. We emphasize this scenario is only possible in the T^- regime. For large E_0 values, corresponding to large Ca_E, the resistive effect from surface tension is negligible, and the only way to obtain a finite equilibrium aspect ratio is therefore by balancing the normal and tangential stresses. Since Q_N is positive, Q_T has to be negative.

3.5 Conclusions

In conclusion, we have developed a transient analysis to quantify droplet deformation under DC electric fields. The full Taylor-Melcher leaky dielectric model is employed

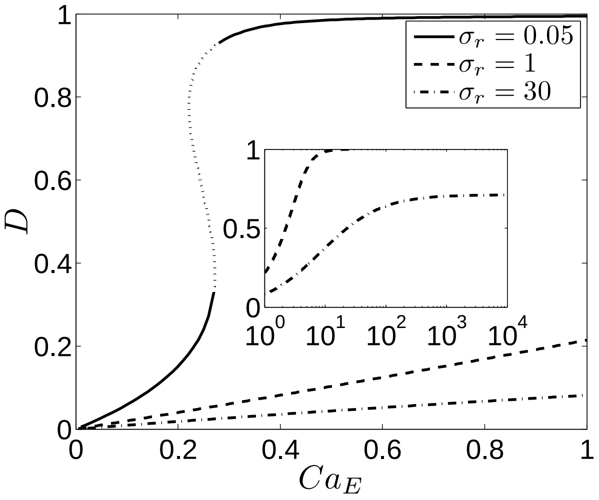

Figure 3.8: The behavior of equilibrium droplet deformation in different regimes. For $\sigma_r = 0.05$, $Q_T > 0$; $\sigma_r = 1$, $Q_T = 0$; $\sigma_r = 30$, $Q_T < 0$. As $Ca_E \to \infty$, an equilibrium shape is only possible in the T^- regime. Other parameters are $\epsilon_r = 10$ and $\mu_r = 1$.

where the charge relaxation time is considered finite. In this framework, instantaneous charge relaxation is treated as a special limiting case. The droplet is assumed to be spheroidal in shape for all times. The main result is an ODE governing the evolution of the droplet aspect ratio. The model is validated by extensively comparing predicted deformation with both previous theoretical and numerical studies, and with experimental data. In particular, the experimental results by Ha and Yang [24], which were obtained with extremely low medium conductivities are well captured by the simulation with the finite-time charge-relaxation model. The model is used to analyze the effects of parameters and stresses on the deformation characteristics. The results demonstrate clearly that in different regimes according to the sign of Q_T, the stresses contribute qualitatively differently to deformation. Last but not least, this work lays the foundation for the study of a more complex problem, namely, vesicle electrodeformation, which is presented in the next chapter.

Chapter 4

A Transient Analysis for Vesicle Electrodeformations

4.1 Introduction

In this chapter, the problem of vesicle electrodeformation is tackled, and a solution is pursued in the similar manner as in the case of the droplet deformation. However, the extension from the droplet to vesicle model is not trivial. In contrast to droplet deformation, vesicle deformation exhibits more complex physical behavior. The difference between droplets and vesicles mainly lies in two aspects. First, contrary to the droplet interface, the lipid membrane is essentially impermeable. When an electric field is applied, charges accumulate at both sides of the lipid membrane, which behaves like a capacitor. Thus an electric potential is built up across the vesicle membrane, which is known as the transmembrane potential (TMP). When the TMP exceeds a critical threshold, 0.2-1 V [10, 62, 75], the membrane becomes permeable and the conductivity of the membrane increases significantly. Second, the mechanical response of a membrane is different from that of a droplet interface in that it consists of two parts: bending resistance and membrane tension. One can easily shows that the bending resistance only has a small contribution to the membrane force such that it could be neglected. However, the membrane tension may have significant effects on the membrane force especially when the deformation is large. In the current work, we consider both effects. A transient analysis is presented to predict both vesicle deformation and relaxation, and to study in-depth their relations with initial membrane tension and pulse length. More importantly, it is found that vesicle relaxation obeys a universal behavior, and is governed by a single timescale that is a function of the vesicle initial radius, the fluid viscosity, and the initial membrane tension. This work has been summarized in a manuscript submitted to Journal of Fluid Mechanics [90].

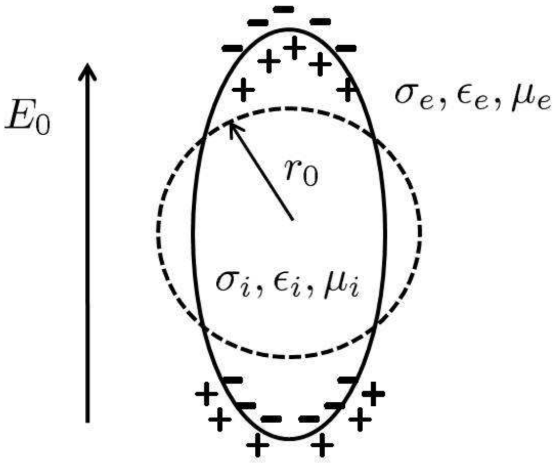

Figure 4.1: A schematic of the problem configuration. The original radius of the vesicle is r_0. The conductivity is denoted by σ, the permittivity is denoted by ϵ, the viscosity is denoted by μ, and the subscripts i and e denote intravesicular and extravesicular, respectively. The strength of the applied electric field is E_0.

4.2 Theory

The problem configuration is identical to that in figure 3.1 in Chapter 3, except that the droplet interface is replaced by an infinitesimally thin membrane (figure 4.1). Consequently, charges of opposite signs are allowed to accumulate on the two sides of the membrane. All notations, as well as the prolate spheroidal coordinate system follow those from Chapter 3. The electrical and mechanical models for the membrane are described later.

4.2.1 The electrical problem

The electric potential is described by the same Laplace equations as in Chapter 3:

$$\nabla^2\phi_i = \nabla^2\phi_e = 0. \tag{4.1}$$

However, at the membrane the matching conditions are modified:

$$\frac{\sigma_e}{h_\xi}\frac{\partial \phi_e}{\partial \xi} = \frac{\sigma_i}{h_\xi}\frac{\partial \phi_i}{\partial \xi} = C_m \frac{\partial \frac{c}{h_\xi}(\phi_e - \phi_i)}{\partial t} + \frac{G_m c}{h_\xi}(\phi_e - \phi_i), \qquad \text{at } \xi = \xi_0. \tag{4.2}$$

Here C_m and G_m denote the membrane capacitance and conductance, respectively. This membrane-charging model is commonly adopted by many previous research [14, 22, 40, 34, 68]. The displacement currents from the electrolytes are not included, which approximation is valid when the Maxwell-Wagner timescale, $T_{MW} = (\epsilon_i + 2\epsilon_e)/(\sigma_i + 2\sigma_e)$, and the charge relaxation timescale, $T_{cr} = \epsilon/\sigma$, are small when compared with the membrane-charging time, $T_{ch} = r_0 C_m (1/\sigma_i + 1/2\sigma_e)$, and the deformation time, $T_d = \mu_e/\epsilon_e E_0^2$. However, the last two times are in general comparable with each other. The first term on the RHS of equation (4.2) represents capacitive charging of the membrane, which includes the effect of membrane deformation. However, the contribution from this effect is usually small, and is neglected in the current analysis for simplicity. Equation (4.2) can be consequently reduced to

$$\frac{\sigma_e}{h_\xi}\frac{\partial \phi_e}{\partial \xi} = \frac{\sigma_i}{h_\xi}\frac{\partial \phi_i}{\partial \xi} = \frac{C_m c}{h_\xi}\frac{\partial (\phi_e - \phi_i)}{\partial t} + \frac{G_m c}{h_\xi}(\phi_e - \phi_i), \qquad \text{at } \xi = \xi_0. \tag{4.3}$$

Equation (4.3) can be further simplified by considering different stages of charging. In the first stage, the TMP, $V_m \equiv (\phi_i - \phi_e)_{\xi=\xi_0}$, grows continuously in magnitude, but the membrane is not permeabilized. Under this condition, G_m is near zero, and equation (4.3) becomes

$$\frac{\sigma_e}{h_\xi}\frac{\partial \phi_e}{\partial \xi} = \frac{\sigma_i}{h_\xi}\frac{\partial \phi_i}{\partial \xi} = \frac{C_m c}{h_\xi}\frac{\partial (\phi_e - \phi_i)}{\partial t}, \qquad \text{at } \xi = \xi_0. \tag{4.4}$$

In the second stage, the maximum TMP reaches the critical threshold, V_c, for electroporation to occur [9, 21, 23, 38, 59, 72, 82]. The membrane becomes permeable to ions, and G_m increases significantly to limit further growth of the TMP. In general, the exact values of V_m and G_m depend on the detailed electroporation conditions and variables such as pore density and pore area [40]. The solution usually requires a complex numerical simulation which is beyond the scope of the theoretical analysis pursued in this paper.

However, a comprehensive model study by Li and Lin [40] showed that the maximum TMP remained at the critical level in the presence of the pulse post-permeabilization. In this work, we adopt an approximate model for this stage. We assume that once the maximum value of V_m reaches V_c, it no longer grows and "freezes" in time. In addition, the membrane is completely permeabilized, and equation (4.3) is replaced by

$$\frac{\sigma_e}{h_\xi}\frac{\partial \phi_e}{\partial \xi} = \frac{\sigma_i}{h_\xi}\frac{\partial \phi_i}{\partial \xi}, \quad V_m = V_c, \qquad \text{at } \xi = \xi_0. \tag{4.5}$$

Note that electroporation only occurs for sufficiently strong electric fields, and equation (4.5) is not needed for some of the cases studied below where V_c is never reached. Far away from the vesicle surface, the electric field is uniform

$$-\nabla \phi_e = E_0 \boldsymbol{z}, \qquad \text{at } \xi \to \infty. \tag{4.6}$$

We also require that ϕ_i remains finite at $\xi = 1$. For initial condition, we solve equations (4.1) and (4.4) with $V_m = 0$.

The general solution of the electric potentials for both the exterior and interior of the vesicle can be obtained following a similar procedure outlined in Chapter 3:

$$\phi_e = E_0 r_0 \left[-\lambda\xi + \alpha Q_1(\xi)\right]\eta, \tag{4.7}$$

$$\phi_i = E_0 r_0 \beta \xi \eta. \tag{4.8}$$

Here, $Q_1(\xi)$ is a 1st-degree Legendre polynomial of the second kind. $\lambda \equiv c/r_0$ is the dimensionless semi-focal length. The coefficients α and β are again obtained by applying the matching conditions. In the absence of electroporation, they are given as

$$\alpha = \frac{\beta + \sigma_r \lambda}{Q_1'(\xi_0)\sigma_r}, \tag{4.9}$$

$$\left[\frac{Q_1(\xi_0)}{Q_1^{'}(\xi_0)\sigma_r}-\xi_0\right]\frac{d\beta}{d\tau}-\left[\frac{Q_1(\xi_0)Q_1^{''}(\xi_0)-Q_1^{'2}(\xi_0)(1-\sigma_r)}{Q_1^{'2}(\xi_0)\sigma_r}\frac{d\xi_0}{d\tau}+\frac{\tau_2}{\tau_1\lambda}\right]\beta$$
$$-\left[\left(\xi_0-\frac{Q_1(\xi_0)}{Q_1^{'}(\xi_0)}\right)\frac{d\lambda}{d\xi_0}+\frac{\lambda Q_1^{''}(\xi_0)Q_1(\xi_0)}{Q_1^{'2}(\xi_0)}\right]\frac{d\xi_0}{d\tau}=0, \qquad (4.10)$$

$$\alpha(0)=\frac{\lambda\xi_0(\sigma_r-1)}{Q_1^{'}(\xi_0)\xi_0\sigma_r-Q_1(\xi_0)}, \qquad \beta(0)=-\lambda\sigma_r+\alpha(0)Q_1^{'}(\xi_0)\sigma_r. \qquad (4.11)$$

Here $\sigma_r \equiv \sigma_e/\sigma_i$ is the conductivity ratio. $\tau_1 \equiv r_0 C_m/\sigma_i$ is a membrane-charging time. $\tau_2 \equiv r_0\mu_e/\Gamma_0$ is a characteristic flow timescale. Γ_0 is the initial membrane tension introduced below. The dimensionless time τ defined as $\tau \equiv t/\tau_2$ has been used. Note that the definition of these times slightly deviates from those used in Chapter 3 due to the difference between droplet and vesicle. However, τ_2 remains formally the same by replacing γ in Chapter 3 with Γ_0.

After the maximum value of V_m reaches the critical threshold, electroporation occurs. α and β are calculated by equation (4.5) which yields

$$\alpha=\frac{-V_c/(E_0 r_0)-\lambda\xi_0(\sigma_r-1)}{Q_1(\xi_0)-Q_1^{'}(\xi_0)\xi_0\sigma_r}, \qquad \beta=-\lambda\sigma_r+\alpha Q_1^{'}(\xi_0)\sigma_r. \qquad (4.12)$$

The expressions for the normal and tangential electrostatic stresses are found in Chapter 3 and not repeated here.

4.2.2 The hydrodynamic problem

The governing equation and boundary conditions for the hydrodynamic problem are the same as in Chapter 3 except that the following stress matching condition is prescribed instead:

$$||\tau\cdot\boldsymbol{n}||=\boldsymbol{f}^{mem}. \qquad (4.13)$$

Here $\boldsymbol{f}^{mem}$ is the surface force density arising from the vesicle membrane. The tensor τ includes contributions from both the hydrodynamic and electrostatic stresses:

$$\tau \equiv -p\mathrm{I}+\mu(\nabla\boldsymbol{v}+\nabla\boldsymbol{v}^T)+\epsilon\boldsymbol{E}\boldsymbol{E}-\frac{1}{2}\epsilon(\boldsymbol{E}\cdot\boldsymbol{E})\mathrm{I}. \qquad (4.14)$$

4.2.3 The membrane-mechanical model

The surface force density at the vesicle membrane essentially consists of two parts [69, 81]

$$\boldsymbol{f}^{mem} = \boldsymbol{f}^{\kappa} + \boldsymbol{f}^{\Gamma}. \tag{4.15}$$

Here $\boldsymbol{f}^{\kappa}$ is the surface force density induced by bending resistance. $\boldsymbol{f}^{\Gamma} = 2\Gamma H\boldsymbol{n} - \nabla_s\Gamma$ is the surface force density induced by the membrane tension. H is the mean curvature, and Γ is the local membrane tension. We can easily verify that $\boldsymbol{f}^{\kappa}$ is several orders of magnitude smaller than $\boldsymbol{f}^{\Gamma}$, and is therefore not included in the current analysis. The local membrane tension, Γ, is calculated by assuming an effective tension which is uniform over the entire membrane [25, 81]. An increase of the homogeneous tension, Γ_h, from the initial tension, Γ_0, leads to an increase in the apparent membrane area [17, 18, 25, 35]:

$$\Delta = \frac{k_B T}{8\pi\kappa}\ln\frac{\Gamma_h}{\Gamma_0} + \frac{\Gamma_h - \Gamma_0}{K_a}. \tag{4.16}$$

Here Δ is the increase in the apparent membrane area relative to the initial spherical state,

$$\Delta = \frac{1}{2}\left(1-\xi_0^{-2}\right)^{-\frac{2}{3}}\left[1-\xi_0^{-2}+\left(\xi_0^2-1\right)^{\frac{1}{2}}\arcsin\left(\xi_0^{-1}\right)\right]-1. \tag{4.17}$$

K_a is the elastic stretching modulus. κ is the bending rigidity. Equation (4.16) indicates that Γ_0, κ, and K_a are the important parameters in determining membrane tension. κ and K_a are usually constants for a specific vesicle type, and their values are often readily obtained from previous work [35, 36, 51]. On the other hand, Γ_0 is specific to an individual vesicle, and its value can not be directly determined from experimental measurements. The relation between Δ and Γ_h for different choices of Γ_0 is shown in figure 4.2. When Δ is small, the membrane area increases through the flattening of the undulations, and Γ_h shows an exponential correlation with Δ. When Δ is sufficiently large, a linear behavior is observed instead, and the membrane area increase is mainly due to elastic stretching. Moreover, a larger Γ_0 always leads to a larger Γ_h for the same value of Δ.

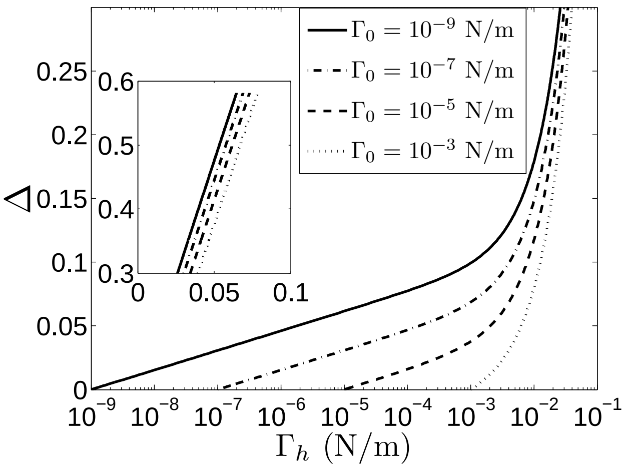

Figure 4.2: The relative increase of the apparent area, Δ, as a function of membrane tension, Γ_h, for different values of initial membrane tension, Γ_0. The inset shows the linear regime for larger Γ_h values.

4.2.4 General solution

A solution for vesicle electrodeformation can be obtained by solving the governing equations of both the electrical and hydrodynamic problems, with the help of the matching conditions. The solution strategy is identical to that presented in Chapter 3, with only differences in the detailed matching conditions for both the electric field and the interfacial forces. For brevity, only the final governing equation for ξ_0 is presented here:

$$\frac{d\xi_0}{d\tau} = -\frac{1}{F}\left[Q_N f_{21}(\xi_0) + Q_T \frac{\mu_r f_{22}(\xi_0) + f_{23}(\xi_0)}{\mu_r f_{14}(\xi_0) + f_{15}(\xi_0)} - \frac{\Gamma_h}{\Gamma_0} f_{24}(\xi_0)\right], \tag{4.18a}$$

$$Q_N = \frac{Ca_E}{\lambda^2}\left[(\lambda - \alpha Q_1^{'}(\xi_0))^2 + (\lambda - \alpha Q_1(\xi_0)/\xi_0)^2 - 2\beta^2/\epsilon_r\right], \tag{4.18b}$$

$$Q_T = \frac{Ca_E}{\lambda^2}\left[(\lambda - \alpha Q_1^{'}(\xi_0))(\lambda - \alpha Q_1(\xi_0)/\xi_0) - \beta^2/\epsilon_r\right]. \tag{4.18c}$$

The functions $f_{14}(\xi_0)$, $f_{15}(\xi_0)$, $f_{21}(\xi_0) - f_{24}(\xi_0)$, and F are the same as those used in Chapter 3, and the detailed expressions are found in the Appendix therein. The factors Q_N and Q_T again arise from the effects of the tangential and normal stresses, respectively. $Ca_E \equiv r_0\epsilon_e E_0^2/\Gamma_0$ is the modified electric capillary number. In the absence of electroporation, the coefficients α and β are given in equations (4.9) and (4.10).

Once the electroporation occurs, equation (4.12) is used instead. Similar to the droplet model, an examination of the three terms in the numerator of equation (4.18a) reveals the contribution from the normal stress, tangential stress, and membrane tension, respectively. The balance between these three terms determines the equilibrium vesicle shape. The above equations are solved until the end of the pulse, $t = t_p$.

In the context of vesicle electrodeformation, the relaxation process is equally important, and is more revealing of the underlying physical processes. The governing equations are presented below. In the absence of electroporation, equation (4.1) is solved without an applied electric field. The resulting equation for ξ_0 remains the same as equation (4.18a). The coefficients of Q_N, Q_T, α, and β are given as

$$Q_N = \frac{\epsilon_e V_c^2}{\lambda^2 r_0 \Gamma_0}\left[\alpha^2\left(Q_1'^2(\xi_0) + Q_1^2(\xi_0)/\xi_0^2\right) - 2\beta^2/\epsilon_r\right], \tag{4.19}$$

$$Q_T = \frac{\epsilon_e V_c^2}{\lambda^2 r_0 \Gamma_0}\left[\alpha^2 Q_1(\xi_0) Q_1'(\xi_0)/\xi_0 - \beta^2/\epsilon_r\right], \tag{4.20}$$

$$\alpha = \frac{\beta}{Q_1'(\xi_0)\sigma_r}, \tag{4.21}$$

$$\left[\frac{Q_1(\xi_0)}{Q_1'(\xi_0)\sigma_r} - \xi_0\right]\frac{d\beta}{d\tau} - \left[\frac{Q_1(\xi_0)Q_1''(\xi_0) - Q_1'^2(\xi_0)(1-\sigma_r)}{Q_1'^2(\xi_0)\sigma_r}\frac{d\xi_0}{d\tau} + \frac{\tau_2}{\tau_1\lambda}\right]\beta = 0, \tag{4.22}$$

$$\alpha(\tau_p) = \frac{V_m(\tau_p)}{V_c(Q_1'(\xi_0)\xi_0\sigma_r - Q_1)}, \qquad \beta(\tau_p) = \frac{V_m(\tau_p)Q_1'(\xi_0)\sigma_r}{V_c(Q_1'(\xi_0)\xi_0\sigma_r - Q_1)}. \tag{4.23}$$

In equation (4.23), the initial conditions for α and β are obtained by solving equations (4.1) and (4.4), and requiring that V_m assumes the value at the end of the pulse. τ_p is the dimensionless time, t_p/τ_2. Note that in this case, although the pulse is switched off, the electric field is in general not zero, due to the capacitive discharging of the membrane. In this case, the TMP will decreases from its peak value to zero on the membrane-charging timescale, T_{ch}.

When electroporation is present, the discharging process is slightly more complex. The full membrane-charging model (4.3) is used. In order to determine the membrane conductance, G_m, we simply assume that it remains unchanged from the moment the pulse ceases, namely,

$$G_m = -\frac{\sigma_e \beta E_0}{\lambda V_c}. \tag{4.24}$$

The resulting equation for ξ_0 again does not formally deviate from equation (4.18a). The coefficients of Q_N, Q_T, α, and β are

$$Q_N = \frac{\epsilon_e V_c^2}{\lambda^2 r_0 \Gamma_0} \left[\alpha^2 \left(Q_1'^2(\xi_0) + Q_1^2(\xi_0)/\xi_0^2\right) - 2\beta^2/\epsilon_r\right], \tag{4.25}$$

$$Q_T = \frac{\epsilon_e V_c^2}{\lambda^2 r_0 \Gamma_0} \left[\alpha^2 Q_1(\xi_0) Q_1'(\xi_0)/\xi_0 - \beta^2/\epsilon_r\right], \tag{4.26}$$

$$\alpha = \frac{\beta}{Q_1'(\xi_0)\sigma_r}, \tag{4.27}$$

$$\begin{aligned}\left[\frac{Q_1(\xi_0)}{Q_1'(\xi_0)\sigma_r} - \xi_0\right]\frac{d\beta}{d\tau} - \Bigg[\frac{Q_1(\xi_0)Q_1''(\xi_0) - Q_1'^2(\xi_0)(1-\sigma_r)}{Q_1'^2(\xi_0)\sigma_r}\frac{d\xi_0}{d\tau} + \frac{\tau_2}{\tau_1 \lambda} \\ - \frac{\tau_2 G_m}{C_m}\left(\frac{Q_1(\xi_0)}{Q_1'(\xi_0)\sigma_r} - \xi_0\right)\Bigg]\beta = 0.\end{aligned} \tag{4.28}$$

4.2.5 A similarity solution for vesicle relaxation

The governing equation for the relaxation process can be further simplified following two considerations. First, we may ignore the membrane-discharging process. The membrane-charging/discharging time, T_{ch}, is on the order of 1 ms, which is in general much shorter than the relaxation time observed in the experiments, namely, a few tens of ms or longer. The relatively small effect of discharging on relaxation is clearly seen in figure 4.3 presented in the following section. Without including the discharging process, the coefficients Q_T and Q_N in equation (4.18a) are simply set to zero. Second, in the membrane-mechanical model (4.16), the first and second term on the RHS represent the effects of undulation unfolding and elastic stretching, respectively. For moderate values of Γ_0, and for small-to-moderate deformations, the second term can be ignored, and the membrane-mechanical model becomes

$$\Delta = \frac{k_B T}{8\pi\kappa}\ln\frac{\Gamma_h}{\Gamma_0}. \tag{4.29}$$

Substituting $Q_T = Q_N = 0$ and equation (4.29) into (4.18a), we obtain

$$\frac{d\xi_0}{d\tau} = \frac{1}{F}\exp(\frac{8\pi\kappa\Delta}{k_BT})f_{24}(\xi_0). \tag{4.30}$$

This equation is conveniently rewritten in terms of the aspect ratio as

$$\frac{d\frac{a}{b}}{d\tau} = -\frac{1}{F}\exp(\frac{8\pi\kappa\Delta}{k_BT})(\xi_0^2-1)^{-\frac{3}{2}}f_{24}(\xi_0). \tag{4.31}$$

Note that in this equation, κ, the bending rigidity, is regarded constant for a specific vesicle type, and μ_r (embedded in F, see Appendix C) is close to 1 as both the fluids are usually aqueous. In addition, Δ, the relative increase of apparent membrane area, depends exclusively on ξ_0, hence a/b according to equation (4.17), and (3.38). Under these assumptions, we observe that equation (4.31) is completely autonomous, and the relaxation process is governed by the dimensionless time, $\tau = t/\tau_2$, where $\tau_2 = r_0\mu_e/\Gamma_0$. This result suggests that the relaxation of vesicles with different initial radius, r_0, and initial tension, Γ_0, obeys a similarity behavior with the proper scaling suggested above. This behavior is demonstrated by both simulation and analysis of previous experimental data below.

4.3 Results

For all results below, we assume the lipid membrane to be made of egg-PC following Riske and Dimova [62] (henceforth abbreviated as $'$RD05$'$) and Sadik *et al.* [64] (henceforth denoted as $'$S11$'$). The bending rigidity is taken to be $\kappa = 2.47 \times 10^{-20}$ J [35]; the elastic modulus, $K_a = 0.14$ N/m [36, 51]; the membrane capacitance, $C_m = 0.01$ F/m^2 [52]; the intravesicular and extravesicular viscosities, $\mu_i = \mu_e = 10^{-3}$ Pa $\cdot$ s; the intravesicular and extravesicular permittivities, $\epsilon_i = \epsilon_e = 7 \times 10^{-10}$ F/m. The critical transmembrane potential is assumed to be $V_c = 1$ V [60].

4.3.1 The effects of Γ_0 and t_p

We begin by examining the effects of Γ_0 on vesicle electrodeformation and relaxation. Figure 4.3 shows the typical system behavior for values of Γ_0 ranging from 10^{-7} – 10^{-3} N/m. The intravesicular and extravesicular conductivities are $\sigma_i = 6 \times 10^{-4}$ S/m and $\sigma_e = 4.5 \times 10^{-4}$ S/m, respectively following RD05. The field strength is $E_0 =$ 1 kV/cm, the pulse length is $t_p = 250$ μs, and the initial radius is $r_0 = 15$ μm. Figure 4.3(a) shows the evolution of V_m at the cathode-facing pole, which demonstrates only a weak dependence on Γ_0. The threshold for electroporation (1 V) is reached just before the end of the pulse, and its effects are present yet negligible. The discharging occurs on the relatively short timescale of 1 ms as we discussed above. Figure 4.3(b) shows the evolution of the aspect ratio, a/b. The discharging process manifests itself as a sudden and slight decrease in the aspect ratio immediately after the pulse ceases; its effects can in general be ignored without significantly altering the relaxation behavior. A smaller value of Γ_0 leads to a larger aspect ratio, and a longer relaxation process. The maximum aspect ratio, $[a/b]_{\max}$, is plotted as a function of Γ_0 in figure 4.3(c). As the initial membrane tension decreases toward zero, the maximum achievable aspect ratio saturates.

The similarity behavior in the relaxation process is demonstrated in figure 4.3(d). The descending branches of the curves ($t > t_p$) shown in figure 4.3(b) are rescaled in terms of $\tau = t/\tau_2$, and shifted horizontally. In comparison, the thick solid curve is obtained by directly solving equation (4.31). The convergence of all curves validates that $\tau_2 = r_0\mu_e/\Gamma_0$ is the single timescale governing vesicle relaxation.

The effects of t_p are examined in figure 4.4. The parameters are the same as in figure 4.3, and we fix Γ_0 at 1×10^{-6} N/m. Figure 4.4(a) shows that a longer pulse consistently leads to greater deformation, and the aspect ratio increases along the same envelope. The relaxation times are approximately the same for all cases, because τ_2 remains unchanged. The discharging process is in general more conspicuous with longer pulses. In figure 4.4(b), the relaxation curves are again shifted horizontally and rescaled with τ_2 to show good agreement with the similarity solution (thick solid line). Note

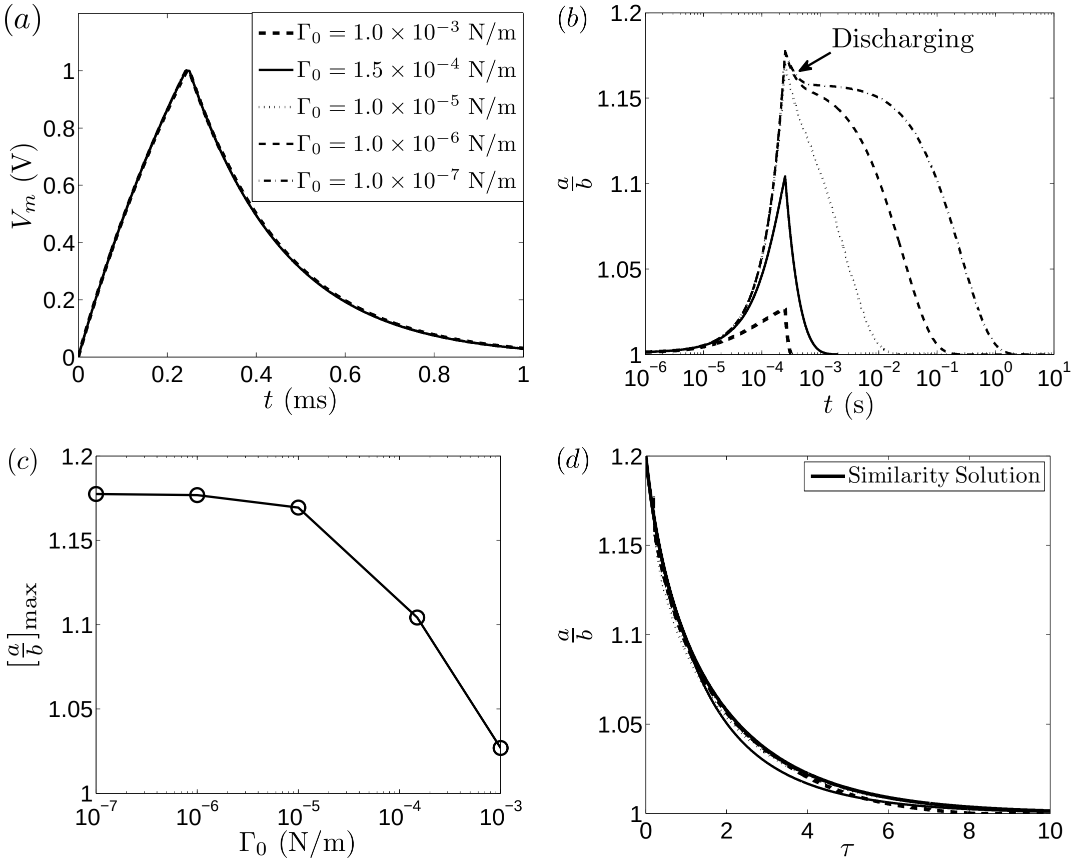

Figure 4.3: Vesicle deformation-relaxation as a function of Γ_0. The governing parameters are $\sigma_i = 6 \times 10^{-4}$ S/m, $\sigma_e = 4.5 \times 10^{-4}$ S/m, $E_0 = 1$ kV/cm, $t_p = 250\,\mu$s, and $r_0 = 15\,\mu$m. (a) The transmembrane potential at the cathode-facing pole. (b) The time-course of the aspect ratio. (c) The maximum aspect ratio as a function of Γ_0. (d) The similarity behavior in relaxation. The descending branches from (b) are rescaled with $\tau = t/\tau_2$. The thick solid curve is directly obtained by integrating equation (4.31).

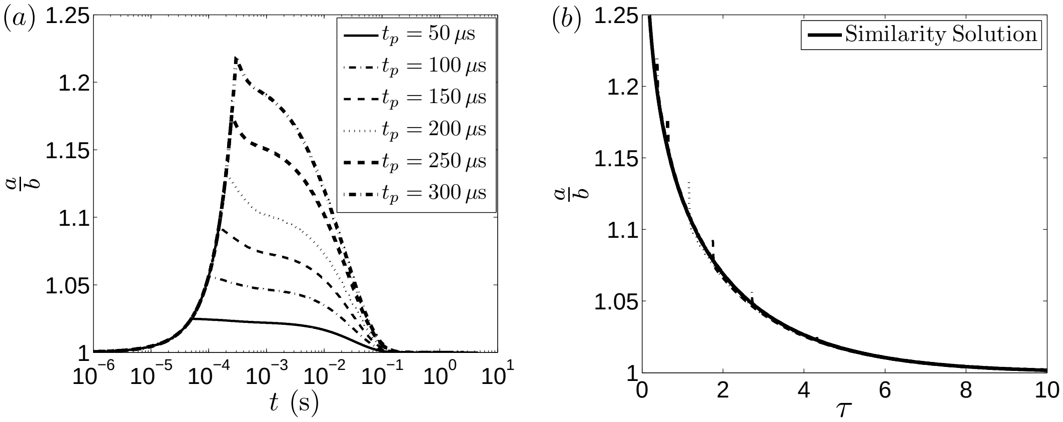

Figure 4.4: Vesicle deformation-relaxation as a function of t_p. The parameters are the same as in figure 4.3. The initial tension is set to be constant, $\Gamma_0 = 1 \times 10^{-6}$ N/m. (a) The time-course of the aspect ratio. (b) The similarity behavior is observed by shifting the relaxation curves with respect to time. The relaxation timescale, $\tau_2 = r_0\mu_e/\Gamma_0$, is the same for all cases. The thick solid curve is directly obtained by integrating equation (4.31).

case #	E_0 (kV/cm)	t_p (μs)	Γ_0 (N/m)
a	1	150	2.79×10^{-4}
b	1	200	3.23×10^{-6}
	1	300*	3.23×10^{-6}
c	1	250	1.67×10^{-4}
d	1	300	1.80×10^{-6}
	1	400*	1.80×10^{-6}
e	2	50	1.80×10^{-4}
	2	80*	1.80×10^{-4}
f	2	100	3.16×10^{-6}
	2	170*	3.16×10^{-6}
g	3	50	6.67×10^{-6}
h	3	100	3.42×10^{-7}

Table 4.1: List of parameters for figure 4.5. For each case, E_0 and t_p are specified according to RD05. Γ_0 is a fitting parameter to obtain best comparison between simulation and data. For cases b, d, e, and f, extended pulse lengths (denoted by star) are also used.

that here because all cases share the same values of τ_2, the collapse of the curves is primarily caused by simple shifting. In other words, the aspect ratio also decreases along a common envelope.

The above results are exemplary and demonstrate the typical system behavior. In general, the relaxation process (in particular the relaxation time) is more appreciably affected by the change in Γ_0 than the deformation process. A wide range of pulsing parameters are studied below, in direct comparison with experimental data from RD05 and S11.

4.3.2 Comparison with experimental data

An extensive comparison of our theoretical prediction with the data from RD05 is presented in figure 4.5. For all eight cases, the initial radius is $r_0 = 15$ μm. The electrical conductivities are $\sigma_i = 6 \times 10^{-4}$ S/m and $\sigma_e = 4.5 \times 10^{-4}$ S/m, respectively, leading to a conductivity ratio of $\sigma_r = 0.75$. Other parameters are listed in table 4.1. All parameters are taken directly from RD05, except for the extended pulse lengths for some cases noted below. For each case, the initial tension, Γ_0, is determined to best fit the experimental data; their values are listed in table 4.1 in the last column. The experimental data are presented as symbols; the theoretical predictions, solid lines. In figures 4.5(a) to 4.5(d), the electric field strength is $E_0 = 1$ kV/cm. For these cases, V_m is predicted to reach V_c at $t = 242$ μs. In figures 4.5(a) and 4.5(c), good agreements are observed between the theoretical prediction and the data. In figures 4.5(b) and 4.5(d), the model results underpredict the maximum aspect ratios. This discrepancy is peculiar: our simulation follows the data accurately during the presence of the pulse, which duration is provided by RD05. After the pulse ceases, the simulation predicts immediate relaxation, whereas the vesicles continued to deform in the experiments, due to some unknown cause. In an attempt to mend this difference, we artificially increase the pulse lengths in the simulation in b and d from 200 and 300 to 300 and 400 μs, respectively. The values for Γ_0 remain unchanged. The results are shown as dashed curves. The model predicts well the data for both the deformation and relaxation processes. Note that although the relaxation curves represented by the solid

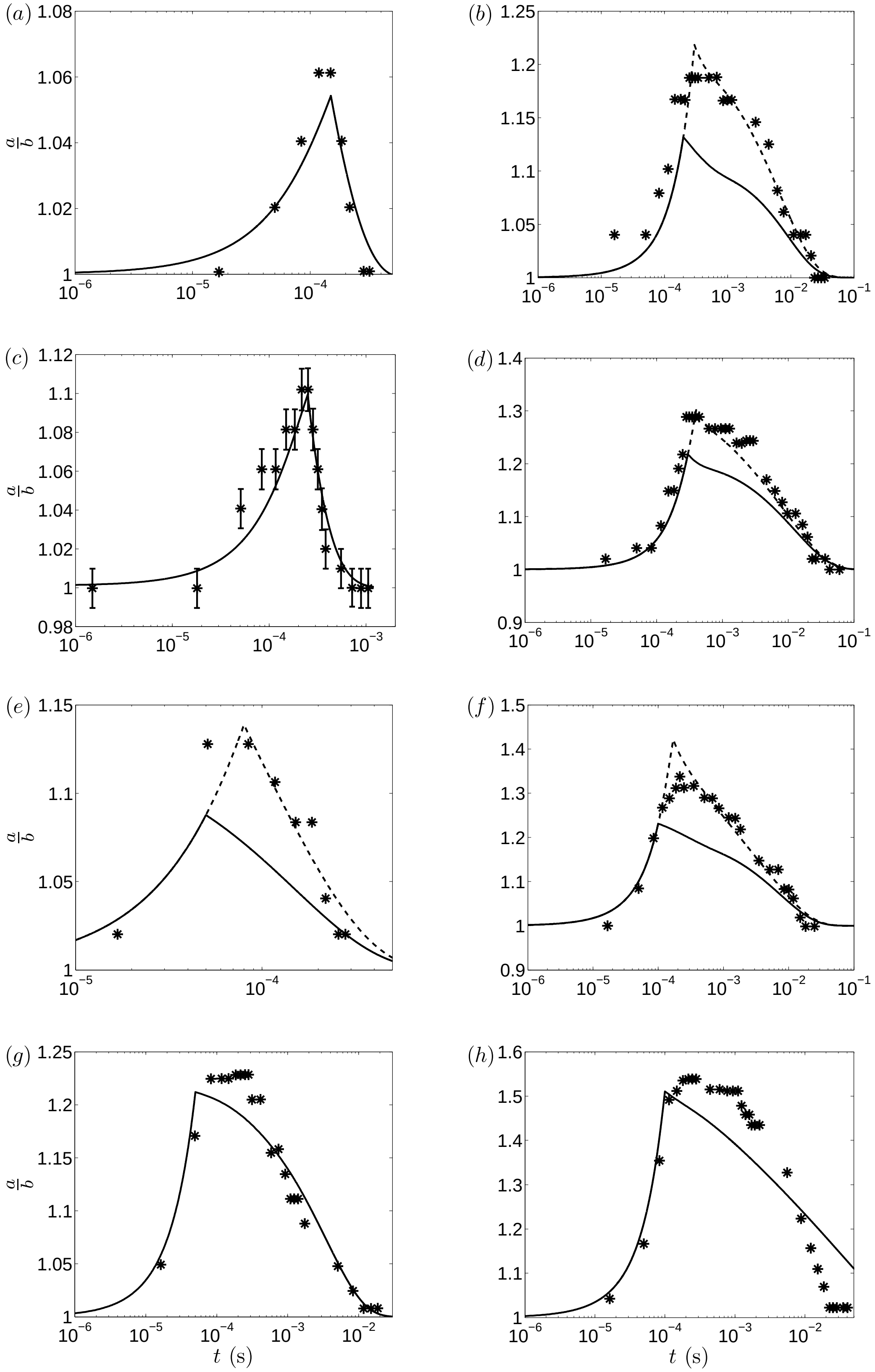

Figure 4.5: Comparison with the deformation-relaxation data from RD05. For all cases, $r_0 = 15\,\mu\text{m}$, $\sigma_i = 6 \times 10^{-4}$ S/m, and $\sigma_e = 4.5 \times 10^{-4}$ S/m. Parameters specific to each case are listed in table 4.1. The data is represented by symbols, and the simulation is represented by solid curves. For cases b, d, e, and f, the dashed lines represent the simulated results with extended pulses (denoted by stars in table 4.1).

and dashed lines look somewhat different due to the semi-log scale on the time axis, they actually follow the same descending envelopes which we have demonstrated in figure 4.4(b) above.

In figures 4.5(e) and 4.5(f), the field strength is increased to be $E_0 = 2$ kV/cm, and the pulse lengths used in RD05 were 50 and 100 μs, respectively. For these cases, our model predicts the occurrence of electroporation around $t = 103$ μs. A similar situation is observed as in figures 4.5(b) and 4.5(d). The solid curves underpredict the maximum aspect ratio. Artificially extending the pulses in e and f to 80 and 170 μs, respectively, leads to much better agreement between the two.

In figures 4.5(g) and 4.5(h), the field strength is further increased to 3 kV/cm, and electroporation is predicted to occur at $t = 66$ μs. The entire deformation-relaxation process is well-captured in g where $t_p = 50$ μs. In figure 4.5(h), where $t_p = 100$ μs, although the model accurately predicts the deformation, the simulated relaxation curve completely deviates from the experimental data. For this case, and for pulses even longer than 100 μs, RD05 (figure 1c therein) exhibits a regime where complex, multi-stage relaxation process was observed. In this regime, the membrane structure is likely severely altered due to electroporation, which process can not be captured by our present model. Further comparison with these data is not pursued.

The similarity behavior in the relaxation process is demonstrated in figure 4.6. The experimental data from figures 4.5(a) to 4.5(g) are shifted horizontally and rescaled with τ_2. For each case, τ_2 is obtained using Γ_0 listed in table 4.1. The thick solid curve is again the similarity solution from equation (4.31), and the results are shown on both semi-log and linear scales in τ. The coefficient of determination is $R^2 = 0.96$. The experimental data from a wide range of parameters demonstrate a universal behavior governed by a single timescale, $\tau_2 = r_0\mu_e/\Gamma_0$. This result is a main contribution of the present work.

We remark that a similar behavior should be observed for droplets, where the initial membrane tension, Γ_0, is replaced by γ, the coefficient of surface tension in τ_2 (cf. the definition of τ_2 in Chapter 3). However, there is a subtle difference between droplet and vesicle relaxation while the coefficient of surface tension is usually a constant, the

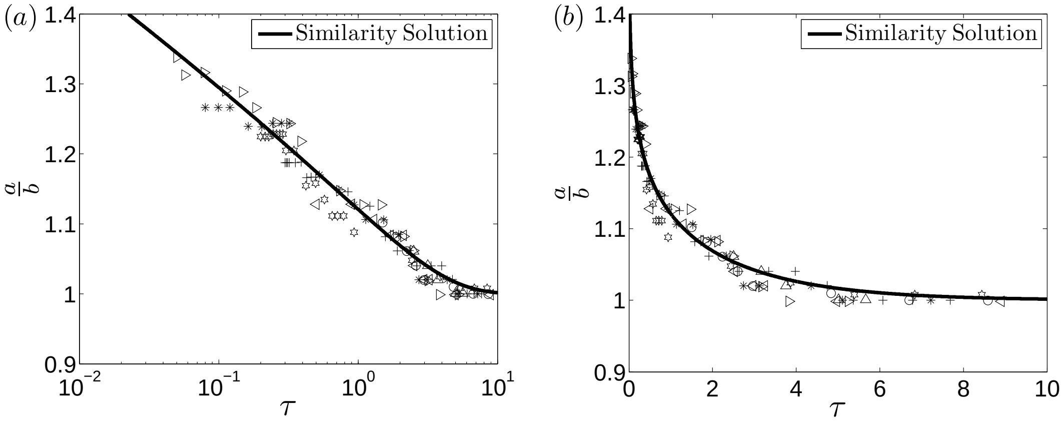

Figure 4.6: The similarity behavior of vesicle relaxation. The experimental data from cases a-g in figure 4.5 are shifted in time, then rescaled by $\tau_2 = r_0\mu_e/\Gamma_0$. They are represented by symbols. The solid curves are calculated with equation (4.31). The same data are shown on both a semi-log (a) and a linear (b) scale. The coefficient of determination is $R^2 = 0.96$.

membrane tension, Γ_h, is not. Nonetheless, as long as Γ_h depends linearly on Γ_0, which is a good approximation for small-to-moderate deformations. The universal behavior in figure 4.6 is expected.

Finally, the model prediction is compared with data from S11. In this work, the deformation is examined at a fixed pulse length of $t_p = 500$ μs, and for five intra-to-extra vesicular conductivity ratios. Only the case of $E_0 = 0.9$ kV/cm is examined, where no or weak electroporation is expected. We do not compare the cases of $E_0 = 2$ and 3 kV/cm in S11, where the vesicles were in the strongly-electroporated regime, and our model no longer applies. The governing parameters are $r_0 = 11.3$ μm and $\sigma_e = 3 \times 10^{-4}$ S/m. The initial membrane tension is chosen to be the same for all vesicles, namely, $\Gamma_0 = 1 \times 10^{-8}$ N/m. Figure 4.7(a) shows the deformation process as a function of time for five conductivity ratios. As σ_r decreases the rate of deformation increases. Except for the case of $\sigma_r = 0.5$, the aspect ratio reaches a plateau before the pulse ends. The time at which the aspect ratio increases saturates with an increasing σ_r. For $\sigma_r = 0.5$, an equilibrium could be reached if the pulse length is extended and sufficiently long (not shown here). In figure 4.7(b), the aspect ratio at $t = t_p$ is shown as a function of $1/\sigma_r$. We choose this representation to facilitate comparison with the data

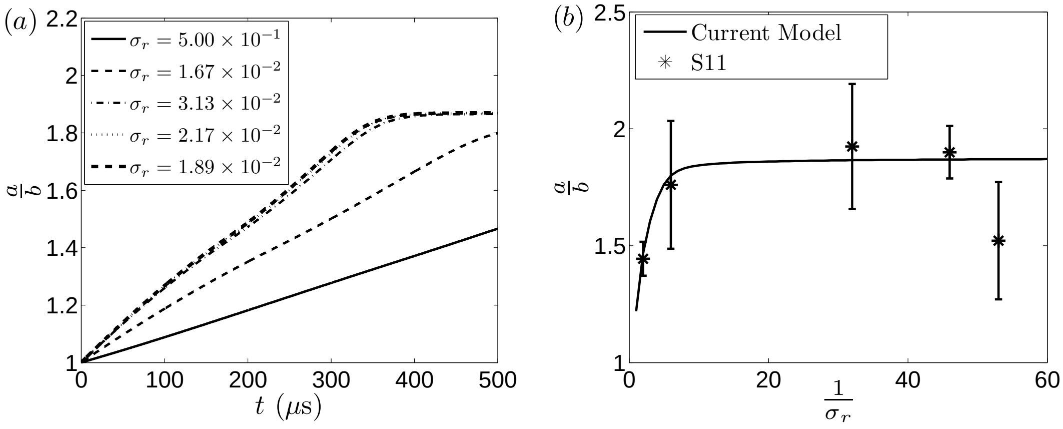

Figure 4.7: Comparison with data from S11. (a) Simulated time-course of the aspect ratio for various conductivity ratios. For all cases $r_0 = 11.3$ μm and $\Gamma_0 = 1 \times 10^{-8}$ N/m. (b) The aspect ratio at $t = 500$ μs as a function of $1/\sigma_r$.

from S11 (symbols), where the definition of the conductivity ratio is σ_i/σ_e. A reasonable agreement is found between the two. The behavior of the simulation and the data is explained by the dependence of the electrical stress on σ_r in S11 (see equation (21) and §4 therein). We do not repeat it here for brevity. The current model represents a significant improvement from that in S11, where the hydrodynamic problem is treated empirically.

Some remarks are appropriate before concluding the section. First, for most cases studied here, the TMP is near the threshold, and the vesicles are expected to experience no or weak electroporation. For this regime, our model is shown to provide a good predictive capability, which demonstrates that the membrane-mechanical model (4.16), although derived assuming no electroporation, can be extended to the weakly-electroporated regime, presumably due to the absence of major structural alterations. Our model is not applicable to the strongly-electroporated regime. Second, the universal scaling law in relaxation observed in figures 4.3, 4.4, and 4.6 is expected to hold regardless of the means of deformation, e.g. via AC/DC electric fields, or via mechanical stretching. Equation (4.31) is applicable to a wide range of relaxation phenomena beyond electrodeformation. Third, the current work suggests that an extensive parametric study on vesicle electrodeformation-relaxation experimentally, in particular in the sub-critical regime where electroporation is avoided, can provide the benefit to further validate our model understanding. A systematic approach can be possibly developed based on this work to map membrane properties.

4.4 Conclusions

In this work, we developed a transient analysis for vesicle electrodeformation. The theory is derived by extending our droplet model in Chapter 3, with the additional consideration of a lipid membrane separating two fluids of arbitrary properties. For the latter, both a membrane-charging and a membrane-mechanical model are supplied. Similar to the droplet model, the main result is also an ODE governing the evolution of the vesicle aspect ratio. The effects of initial membrane tension and pulse length are examined. The initial membrane tension affects the relaxation process much more significantly than the deformation process, in particular when its value is small. The model prediction is extensively compared with experimental data from Riske and Dimova [62] and Sadik *et al.* [64], and is shown to accurately capture the system behavior in the regime of no or weak electroporation. More importantly, the comparison reveals that vesicle relaxation obeys a universal behavior, and is governed by a single timescale that is a function of the vesicle initial radius, the fluid viscosity, and the initial membrane tension. This behavior is regardless of the means of deformation, either via AC/DC electric field, or via mechanical stretching. This universal scaling law is a main contribution of the current work, and can be used to calculate membrane properties from experimental data.

Chapter 5

Conclusions

In this work, we have developed theoretical models to study the dynamics of fluid motion under electric fields. The Taylor-Melcher leaky dielectric model is employed to investigate the problems of EHD instability, droplet electrodeformation, and vesicle electrodeformation.

In the first, EHD instability, we have systematically analyzed the stability of electrified and stratified fluids. Analytical dispersion relations for two- and three-layer problems have been obtained by applying simultaneously the electrical and the hydrodynamic transfer relations. Both new results and those from previous work are derived as special cases of the general solutions presented. This work provides a unified approach to tackle a wide class of EHD instability phenomena.

In the second, droplet electrodeformation, we have developed a transient analysis for droplet deformations under DC electric fields. The finite charge relaxation is considered in order to generalize the analysis. The results are well applicable to explain experimental measurements. In this framework, instantaneous charge relaxation is treated as a special limiting case. The main result is an ODE governing the evolution of the droplet aspect ratio. Based on this model, the effects of parameters and stresses on the deformation characteristics are systematically investigated. The analysis reveals the general behavior of droplet electrodeformation.

In the third, vesicle electrodeformation, we have constructed a transient theory to quantify the vesicle deformation and relaxation under DC electric fields. The analysis extends from our droplet deformation model by including the effects of membrane charging and membrane tension. Similar to the droplet model, the main result is also an ODE governing the evolution of the vesicle aspect ratio. Predictions from both vesicle deformation and relaxation are extensively compared with experimental data. The model accurately captures the system behavior in the regime of no or weak electroporation. More importantly, the results indicate that vesicle relaxation obeys a universal behavior, and is governed by a single timescale that is a function of the vesicle initial radius, the fluid viscosity, and the initial membrane tension. Our theory provides an important means to study vesicle electrodeformation and membrane properties and responses.

In summary, the tasks accomplished in this work are important steps toward the understanding of complex electric-field-driven flows. The analytical tools provide quantitative prediction capabilities, and can be further used to study the problems with in-depth understanding.

Appendix A

The derivation of the transfer relations

The transfer relations are derived by considering a generic fluid layer with density ρ, viscosity μ, and a thickness $\triangle$, governed by the linearized normal mode equations for both the electric potential and the stream function (see (2.7), (2.8) in the proper text):

$$\left(D_y^2 - k^2\right)\hat{\phi} = 0, \tag{A.1}$$

$$\left(D_y^2 - \delta^2\right)\left(D_y^2 - k^2\right)\hat{\psi} = 0, \quad \delta \equiv \left[k^2 + \frac{s\rho}{\mu}\right]^{\frac{1}{2}}. \tag{A.2}$$

These equations are subject to the boundary conditions:

$$\hat{\phi}(y=0) = \hat{\phi}^\beta, \quad \hat{\phi}(y=\triangle) = \hat{\phi}^\alpha, \tag{A.3}$$

$$D_y\hat{\psi}(y=0) = \hat{u}^\beta, \quad D_y\hat{\psi}(y=\triangle) = \hat{u}^\alpha, \tag{A.4}$$

$$-ik\hat{\psi}(y=0) = \hat{v}^\beta, \quad -ik\hat{\psi}(y=\triangle) = \hat{v}^\alpha. \tag{A.5}$$

Note that these boundary conditions are *non-specific*, in contrast to the *specific* conditions given in (2.9-2.12) in the proper text. The electrical transfer relation (2.13) is obtained by solving (A.1) with (A.3). The hydrodynamic transfer relation (2.14) is obtained by solving (A.2) with (A.4) and (A.5). For further details, we refer the readers to Melcher (1981, §2.16, §7.19).

Appendix B

Three layers in the limit of a, $\sigma_r \to \infty$

The dispersion relations for three layers in the limit of a, $\sigma_r \to \infty$ are derived from (2.33), (2.34). Here we rearrange them to facilitate comparison with the results from [49]:

$$\begin{aligned}
&\frac{\begin{aligned}&[2ik(\mu_a-\mu_b)(k-\delta_a)+is\rho_a(1+\tanh(kh))]\\ &\qquad\times[2ik(\mu_a-\mu_b)(k\tanh(kh)-\delta_b\tanh(\delta_b h))-is\rho_b(1+\tanh(kh))]\end{aligned}}{\rho_a(\delta_b\tanh(\delta_b h)-k\tanh(kh))+\rho_b(\delta_a-k)}\\
&+2sk(\mu_a-\mu_b)(1-\tanh(kh))+s^2k^{-1}(\rho_a+\rho_b\tanh(kh))-k\epsilon_b E_{app}^2\tanh(kh)+\gamma k^2=0,
\end{aligned} \tag{B.1a}$$

$$\begin{aligned}
&\frac{\begin{aligned}&[2ik(\mu_a-\mu_b)(k-\delta_a)+is\rho_a(1+\coth(kh))]\\ &\qquad\times[2ik(\mu_a-\mu_b)(k\coth(kh)-\delta_b\coth(\delta_b h))-is\rho_b(1+\coth(kh))]\end{aligned}}{\rho_a(\delta_b\coth(\delta_b h)-k\coth(kh))+\rho_b(\delta_a-k)}\\
&+2sk(\mu_a-\mu_b)(1-\coth(kh))+s^2k^{-1}(\rho_a+\rho_b\coth(kh))-k\epsilon_b E_{app}^2\coth(kh)+\gamma k^2=0,
\end{aligned} \tag{B.1b}$$

where

$$h = b/2, \quad E_{app} = \phi_o/b. \tag{B.1c}$$

Here (B.1a) is for the kink mode, and (B.1b) is for the sausage mode. Note that because the outer layers are infinitely more conductive, all of the potential drop is in the inner layer ($E_{app} = \phi_o/b$). Equations (B.1a), (B.1b) recover (5.23) in [49].

Appendix C

Expressions of $f_{11}(\xi_0) - f_{15}(\xi_0)$, $f_{21}(\xi_0) - f_{24}(\xi_0)$, and F

The functions $f_{11}(\xi_0) - f_{15}(\xi_0)$ in equation (3.34) are given in the following expressions:

$$f_{11}(\xi_0) = \int \frac{G_3(\eta)\eta}{(\xi_0^2 - \eta^2)} d\eta, \tag{C.1}$$

$$f_{12}(\xi_0) = \frac{1}{\xi_0^2 - 1} \left\{ \int \frac{G_3(\eta)\eta}{(\xi_0^2 - \eta^2)} \left(\frac{(1 - 3\eta^2)}{(\xi_0^2 - \eta^2)} - 3 \right) d\eta \right\}, \tag{C.2}$$

$$f_{13}(\xi_0) = \frac{G_3^{''}(\xi_0) G_5^{'}(\xi_0) - G_3^{'}(\xi_0) G_5^{''}(\xi_0)}{2N} \cdot f_{11}(\xi_0), \tag{C.3}$$

$$f_{14}(\xi_0) = -\xi_0 H_3^{'}(\xi_0) \int \frac{G_3(\eta)\eta}{(\xi_0^2 - \eta^2)^2} d\eta + \frac{1}{2} H_3^{''}(\xi_0) f_{11}(\xi_0), \tag{C.4}$$

$$\begin{aligned} f_{15}(\xi_0) = {} & -\frac{H_3^{'}(\xi_0) \left[G_3(\xi_0) G_5^{''}(\xi_0) - G_3^{''}(\xi_0) G_5(\xi_0) \right]}{2N} f_{11}(\xi_0) \\ & + \xi_0 H_3^{'}(\xi_0) \int \frac{G_3(\eta)\eta}{(\xi_0^2 - \eta^2)^2} d\eta. \end{aligned} \tag{C.5}$$

The functions $f_{21}(\xi_0) - f_{24}(\xi_0)$ and F in equation (3.35a) are given in the following expressions:

$$f_{21}(\xi_0) = \frac{1}{2} \xi_0^2 \int \frac{(\eta^2 - 1)(3\eta^2 - 1)}{(\xi_0^2 - \eta^2)} d\eta, \tag{C.6}$$

$$\begin{aligned} f_{22}(\xi_0) = \xi_0 f_{11}(\xi_0) \Bigg[& -H_3^{'}(\xi_0) \int \frac{(1 - 3\eta^2)(\xi_0^2 - 3\xi_0^2\eta^2 + 2\eta^4)}{(\xi_0^2 - \eta^2)^2} d\eta \\ & + 3\xi_0 H_3(\xi_0) \int \frac{1 - 3\eta^2}{(\xi_0^2 - \eta^2)} d\eta \Bigg], \end{aligned} \tag{C.7}$$

$$\begin{aligned} f_{23}(\xi_0) = \xi_0 f_{11}(\xi_0) \Bigg[& -\frac{49(1-3\xi_0^2)G_3(\xi_0)H_3^{'}(\xi_0)}{30N} \\ & + H_3^{'}(\xi_0) \int \frac{(1-3\eta^2)(\xi_0^2 - 3\xi_0^2\eta^2 + 2\eta^4)}{(\xi_0^2-\eta^2)^2} d\eta \Bigg], \end{aligned} \tag{C.8}$$

$$f_{24}(\xi_0) = \xi_0^3(1-\xi_0^{-2})^{\frac{5}{6}} \int \frac{3\eta^2-1}{(\xi_0^2-\eta^2)^{\frac{3}{2}}} d\eta + \xi_0(1-\xi_0^{-2})^{-\frac{1}{6}} \int \frac{3\eta^2-1}{\sqrt{\xi_0^2-\eta^2}} d\eta, \tag{C.9}$$

$$F = -\frac{2}{3}\left(f_{25}(\xi_0) + f_{26}(\xi_0)/\mu_r\right), \tag{C.10}$$

where

$$\begin{aligned} f_{25}(\xi_0) = & -\frac{f_{22}(\xi_0)}{\xi_0 f_{11}(\xi_0)} \frac{(\mu_r-1)f_{12}(\xi_0) + f_{13}(\xi_0)}{\mu_r f_{14}(\xi_0) + f_{15}(\xi_0)} - 3\xi_0 \int \frac{3\eta^2-1}{(\xi_0^2-\eta^2)} d\eta \\ & - \frac{\xi_0}{\xi_0^2-1} \int \frac{(2\xi_0^2-\eta^2-1)(1-3\eta^2)^2}{(\xi_0^2-\eta^2)^2} d\eta, \end{aligned} \tag{C.11}$$

$$\begin{aligned} f_{26}(\xi_0) = & -\frac{f_{23}(\xi_0)}{\xi_0 f_{11}(\xi_0)} \frac{(\mu_r-1)f_{12}(\xi_0) + f_{13}(\xi_0)}{\mu_r f_{14}(\xi_0) + f_{15}(\xi_0)} - \frac{49(1-3\xi_0^2)G_3^{'}(\xi_0)}{30N} \\ & + \frac{\xi_0}{\xi_0^2-1} \int \frac{(2\xi_0^2-\eta^2-1)(1-3\eta^2)^2}{(\xi_0^2-\eta^2)^2} d\eta. \end{aligned} \tag{C.12}$$

Bibliography

[1] O. O. Ajayi. A note on Taylor's electrohydrodynamic theory. *Proc. R. Soc. Lond. A*, 364:499–507, 1978.

[2] R. S. Allan and S. G. Mason. Particle behaviour in shear and electric fields. I. Deformation and burst of fluid drops. *Proc. R. Soc. Lond. A*, 267:45–61, 1962.

[3] S. Aranda, K. A. Riske, R. Lipowsky, and R. Dimova. Morphological transitions of vesicles induced by alternating electric fields. *Biophys. J.*, 95:L19–L21, 2008.

[4] O. A. Basaran. Small-scale free surface flows with breakup: drop formation and emerging applications. *AIChE J.*, 48(9):1842–1848, 2002.

[5] J. C. Baygents and F. Baldessari. Electrohydrodynamic instability in a thin fluid layer with an electrical conductivity gradient. *Phys. Fluids*, 10(1):301–311, 1998.

[6] J. C. Baygents, N. J. Rivette, and H. A. Stone. Electrohydrodynamic deformation and interaction of drop pairs. *J. Fluid Mech.*, 368:359–375, 1998.

[7] N. Bentenitis and S. Krause. Droplet deformation in dc electric fields: the extended leaky dielectric model. *Langmuir*, 21:6194–6209, 2005.

[8] C.-C. Chang and R.-J. Yang. Electrokinetic mixing in microfluidic systems. *Microfluid. Nanofluid.*, 3:501–525, 2007.

[9] D. C. Chang and T. S. Reese. Changes in membrane structure induced by electroporation as revealed by rapid-freezing electron microscopy. *Biophys. J.*, 58:1–12, 1990.

[10] C. Chen, S. W. Smye, and M. P. Robinson. Membrane electroporation theories: a review. *Med Biol Eng Comput*, 44:5–14, 2006.

[11] C.-H. Chen, H. Lin, S. K. Lele, and J. G. Santiago. Convective and absolute electrokinetic instability with conductivity gradients. *J. Fluid Mech.*, 524:263–303, 2005.

[12] R. V. Craster and O. K. Matar. Electrically induced pattern formation in thin leaky dielectric films. *Phys. Fluids*, 17:032104, 2005.

[13] G. Dassios, M. Hadjinicolaou, and A. C. Payatakes. Generalized eigenfunctions and complete semiseparable solutions for Stokes flow in spheroidal coordinates. *Q. Appl. Math.*, 52(1):157–191, 1994.

[14] K. A. Debruin and W. Krassowska. Modeling electroporation in a single cell. I. Effects of field strength and rest potential. *Biophys. J.*, 77:1213–1224, 1999.

[15] R. Dimova, K. A. Riske, Aranda S., N. Bezlyepkina, R. L. Knorr, and R. Lipowsky. Giant vesicles in electric fields. *Soft Matter*, 3:817–827, 2007.

[16] N. Dubash and A. J. Mestel. Behaviour of a conducting drop in a highly viscous fluid subject to an electric field. *J. Fluid Mech.*, 581:469–493, 2007.

[17] E. Evans. Entropy-driven tension in vesicle membranes and unbinding of adherent vesicles. *Langmuir*, 7:1900–1908, 1991.

[18] E. Evans and W. Rawicz. Entropy-driven tension and bending elasticity in condensed-fluid membranes. *Phys. Rev. Lett.*, 64(17):2094–2097, 1990.

[19] J. Q. Feng. Electrohydrodynamic behaviour of a drop subjected to a steady uniform electric field at finite electric Reynolds number. *Proc. R. Soc. Lond. A*, 455:2245–2269, 1999.

[20] J. Q. Feng and T. C. Scott. A computational analysis of electrohydrodynamics of a leaky dielectric drop in an electric field. *J. Fluid Mech.*, 311:289–326, 1996.

[21] M. L. Fernandez, G. Marshall, F. Sagues, and R. Reigada. Structural and kinetic molecular dynamics study of electroporation in cholesterol-containing bilayers. *J. Phys. Chem. B*, 114(20):6855–6865, 2010.

[22] C. Grosse and H. P. Schwan. Celluar membrane potentials induced by alternating fields. *Biophys. J.*, 63(6):1632–1642, 1992.

[23] A. A. Gurtovenko and I. Vattulainen. Pore formation coupled to ion transport through lipid membranes as induced by transmembrane ionic charge imbalance: atomistic molecular dynamics study. *J. Am. Chem. Soc.*, 127:17570–17571, 2005.

[24] J.-W. Ha and S.-M. Yang. Deformation and breakup of Newtonian and non-Newtonian conducting drops in an electric field. *J. Fluid Mech.*, 405:131–156, 2000.

[25] W. Helfrich and R. M. Servuss. Undulations, steric interaction and cohension of fluid membranes. *Il Nuvo Cimento*, 3D:137–151, 1984.

[26] T. Hirata, T. Kikuchi, T. Tsukada, and M. Hozawa. Finite element analysis of electrohydrodynamic time-dependent deformation of dielectric drop under uniform DC electric field. *J. Chem. Engng Japan*, 33(1):160–167, 2000.

[27] J. F. Hoburg and J. R. Melcher. Internal electrohydrodynamic instability and mixing of fluids with orthogonal field and conductivity gradients. *J. Fluid Mech.*, 73:333–351, 1976.

[28] J. F. Hoburg and J. R. Melcher. Electrohydrodynamic mixing and instability induced by colinear fields and conductivity gradients. *Phys. Fluids*, 20(6):903–911, 1977.

[29] H. Hyuga, K. Jr. Kinosita, and N. Wakabayashi. Deformation of vesicles under the influence of strong electric fields. *Jpn. J. Appl. Phys.*, 30(5):1141–1148, 1991.

[30] H. Hyuga, K. Jr. Kinosita, and N. Wakabayashi. Deformation of vesicles under the influence of strong electric fields II. *Jpn. J. Appl. Phys.*, 30(6):1333–1335, 1991.

[31] S. Kakorin, T. Liese, and E. Neumann. Membrane curvature and high-field electroporation of lipid bilayer vesicles. *J. Phys. Chem. B*, 107:10243–10251, 2003.

[32] S. Kanazawa, Y. Takahashi, and Y. Nomoto. Emulsification and demulsification processes in liquid-liquid system by electrostatic atomization technique. *IEEE Trans. Ind. Appl.*, 44(4):1084–1089, 2008.

[33] P. Kim, C. Duprat, S. S. H. Tsai, and H. A. Stone. Selective spreading and jetting of electrically driven dielectric films. *Phys. Rev. Lett.*, 107:034502, 2011.

[34] W. Krassowska and P. D. Filev. Modeling electroporation in a single cell. *Biophys. J.*, 92:404–417, 2007.

[35] M. Kummrow and W. Helfrich. Deformation of giant lipid vesicles by electric fields. *Phys. Rev. A*, 44(12):8356–8360, 1991.

[36] R. Kwok and E. Evans. Thermoelasticity of large lecithin bilayer vesicles. *Biophys. J.*, 35:637–652, 1981.

[37] Etienne Lac and G. M. Homsy. Axisymmetric deformation and stability of a viscous drop in a steady electric field. *J. Fluid Mech.*, 590:239–264, 2007.

[38] H. Leontiadou, A. E. Mark, and S. J. Marrink. Molecular dynamics simulations of hydrophilic pores in lipid bilayers. *Biophys. J.*, 86:2156–2164, 2004.

[39] F. Li, O. Ozen, N. Aubry, D. T. Papageorgiou, and P. G. Petropoulos. Linear stability of a two-fluid interface for electrohydrodynamic mixing in a channel. *J. Fluid Mech.*, 583:347–377, 2007.

[40] J. Li and H. Lin. Numerical simulation of molecular uptake via electroporation. *Bioelectrochemistry*, 82:10–21, 2011.

[41] H. Lin. Electrokinetic instability in microchannel flows: A review. *Mech. Res. Commun.*, 36:33–38, 2009.

[42] H. Lin, B. D. Storey, M. H. Oddy, C.-H. Chen, and J. G. Santiago. Instability of electrokinetic microchannel flows with conductivity gradients. *Phys. Fluids*, 16(6):1922–1935, 2004.

[43] H. Lin, B. D. Storey, and J. G. Santiago. A depth-averaged electrokinetic flow model for shallow microchannels. *J. Fluid Mech.*, 608:43–70, 2008.

[44] J. R. Melcher. *Continuum Electromechanics.* MIT Press, Cambridge, 1981.

[45] J. R. Melcher and M. S. Firebaugh. Traveling-wave bulk electroconvection induced across a temperature gradient. *Phys. Fluids*, 10:1178–1185, 1967.

[46] J. R. Melcher and W. J. Schwarz. Interfacial relaxation overstability in a tangential electric field. *Phys. Fluids*, 11(12):2604–2616, 1968.

[47] J. R. Melcher and C. V. Smith. Electrohydrodynamic charge relaxation and interfacial perpendicular-field instability. *Phys. Fluids*, 12(4):778–790, 1969.

[48] J. R. Melcher and G. I. Taylor. Electrohydrodynamics: a review of the role of interfacial shear stress. *Annu. Rev. Fluid Mech.*, 1:111–146, 1969.

[49] D. H. Michael and M. E. O'Neill. Electrohydrodynamic instability in plane layers of fluid. *J. Fluid Mech.*, 41:571–580, 1970.

[50] M. J. Miksis. Shape of a drop in an electric field. *Phys. Fluids*, 24(11):1967–1972, 1981.

[51] D. Needham. Cohesion and permeability of lipid bilayer vesicles. In E. A. Disalvo and S. A. Simon, editors, *Permeability and Stability of Lipid Bilayers*, pages 49–76. CRC Press, Boca Raton, FL, 1995.

[52] D. Needham and R. M. Hochmuth. Electro-mechanical permeabilization of lipid vesicles. Role of membrane tension and compressibility. *Biophys. J.*, 55:1001–1009, 1989.

[53] G. Niggemann, M. Kummrow, and W. Helfrich. The bending rigidity of phosphatidylcholine bilayers: Dependences on experimental method, sample cell sealing and temperature. *J. Phys. II France*, 5:413–425, 1995.

[54] M. H. Oddy, J. G. Santiago, and J. C. Mikkelsen. Electrokinetic instability micromixing. *Anal. Chem.*, 73:5822–5832, 2001.

[55] O. Ozen, N. Aubry, D. T. Papageorgiou, and P. G. Petropoulos. Electrohydrodynamic linear stability of two immiscible fluids in channel flow. *Electrochim. Acta*, 51:5316–5323, 2006.

[56] O. Ozen, N. Aubry, D. T. Papageorgiou, and P. G. Petropoulos. Monodisperse drop formation in square microchannels. *Phys. Rev. Lett.*, 96:144501, 2006.

[57] D. T. Papageorgiou and P. G. Petropoulos. Generation of interfacial instabilities in charged electrified viscous liquid films. *J. Eng. Math.*, 50:223–240, 2004.

[58] J. K. Park, J. C. Ryu, W. K. Kim, and K. H. Kang. Effect of electric field on electrical conductivity of dielectric liquids mixed with polar additives: DC conductivity. *J. Phys. Chem. B*, 113:12271–12276, 2009.

[59] U. Pliquett, R. P. Joshi, V. Sridhara, and K. H. Schoenbach. High electrical field effects on cell membranes. *Bioelectrochemistry*, 70:275–282, 2007.

[60] T. Portet and R. Dimova. A new method for measuring edge tensions and stability of lipid bilayers: effect of membrane composition. *Biophys. J.*, 99:3264–3273, 2010.

[61] J. D. Posner and J. G. Santiago. Convective instability of electrokinetic flows in a cross-shaped microchannel. *J. Fluid Mech.*, 555:1–42, 2006.

[62] K. A. Riske and R. Dimova. Electro-deformation and poration of giant vesicles viewed with high temporal resolution. *Biophys. J.*, 88:1143–1155, 2005.

[63] K. A. Riske and R. Dimova. Electric pulses induce cylindrical deformations on giant vesicles in salt solutions. *Biophys. J.*, 91:1778–1786, 2006.

[64] M. M. Sadik, J. Li, J. W. Shan, D. I. Shreiber, and H. Lin. Vesicle deformation and poration under strong dc electric fields. *Phys. Rev. E*, 83:066316, 2011.

[65] P. F. Salipante and P. M. Vlahovska. Electrohydrodynamics of drops in strong uniform dc electric fields. *Phys. Fluids*, 22:112110, 2010.

[66] H. Sato, N. Kaji, T. Mochizuki, and Y. H. Mori. Behavior of oblately deformed droplets in an immiscible dielectric liquid under a steady and uniform field. *Phys. Fluids*, 18:127101, 2006.

[67] D. A. Saville. Electrohydrodynamics: The taylor-melcher leaky dielectric model. *Annu. Rev. Fluid Mech.*, 29:27–64, 1997.

[68] H. P. Schwan. Dielectrophoresis and rotation of cells. In E. Neumann, A. E. Sowers, and C. A. Jordan, editors, *Electroporation and electrofusion in cell biology*. Plenum Press, 1989.

[69] U. Seifert. Configurations of fluid membranes and vesicles. *Adv. Phys.*, 46:13–137, 1997.

[70] J. D. Sherwood. Breakup of fluid droplets in electric and magnetic fields. *J. Fluid Mech.*, 188:133–146, 1988.

[71] B. D. Storey, B. S. Tilley, H. Lin, and J. G. Santiago. Electrokinetic instabilities in thin microchannels. *Phys. Fluids*, 17:018103, 2005.

[72] M. Tarek. Membrane electroporation: a molecular dynamics simulation. *Biophys. J.*, 88:4045–4053, 2005.

[73] G. I. Taylor. Disintegration of water drops in an electric field. *Proc. R. Soc. Lond. A*, 280:383–397, 1964.

[74] G. I. Taylor. Studies in electrohydrodynamics. i. the circulation produced in a drop by an electric field. *Proc. R. Soc. Lond. A*, 291:159–166, 1966.

[75] J. Teissie and T. Y. Tsong. Electric field induced transient pores in phopholipid bilayer vesicles. *Biochemistry.*, 20:1548–1554, 1981.

[76] R. M. Thaokar and V. Kumaran. Electrohydrodynamic instability of the interface between two fluids confined in a channel. *Phys. Fluids*, 17:084104, 2005.

[77] S. Torza, R. G. Cox, and S. G. Mason. Electrohydrodynamic deformation and burst of liquid drops. *Phil. Trans. R. Soc. Lond. A*, 269:295–319, 1971.

[78] A. K. Uguz and N. Aubry. Quantifying the linear stability of a flowing electrified two-fluid layer in a channel for fast electric times for normal and parallel electric fields. *Phys. Fluids*, 20:092103, 2008.

[79] A. K. Uguz, O. Ozen, and N. Aubry. Electric field effect on a two-fluid interface instability in channel flow for fast electric times. *Phys. Fluids*, 20:031702, 2008.

[80] O. Vizika and D. A. Saville. The electrohydrodynamic deformation of drops suspended in liquids in steady and oscillatory electric fields. *J. Fluid Mech.*, 239:1–21, 1992.

[81] P. M. Vlahovska, R. S. Gracia, S. Aranda-Espinoza, and R. Dimova. Electrohydrodynamic model of vesicle deformation in alternating electric fields. *Biophys. J.*, 96:4789–4803, 2009.

[82] J. Wohlert, W. K. den Otter, O. Edholm, and W. J. Briels. Free energy of a trans-membrane pore calculated from atomistic molecular dynamics simulations. *J. Chem. Phys.*, 124:154905, 2006.

[83] P. K. Wong, W. Tan, and C. M. Ho. Cell relaxation after electrodeformation: effect of latrunculin a on cytoskeletal actin. *Biomech. J.*, 38:529–535, 2005.

[84] Y. Wu and R. L. Clark. Electrohydrodynamic atomization: a versatile process for preparing materials for biomedical applications. *J. Biomater. Sci. Polymer Edn*, 19(5):573–601, 2008.

[85] M. Yazdani and J. Seyed-Yagoobi. Heat transfer augmentation of parallel flows by means of electric conduction phenomenon in macro- and micro-scales. *ASME J. Heat Transfer*, 132:062402, 2010.

[86] J. D. Zahn and V. Reddy. Two phase micromixing and analysis using electrohydrodynamic instabilities. *Microfluid. Nanofluid.*, 2:399–415, 2006.

[87] R. E. Zelazo and J. R. Melcher. Dynamic interactions of monomolecular films with imposed electric fields. *Phys. Fluids*, 17(1):61–72, 1974.

[88] J. Zhang, J. D. Zahn, and H. Lin. A general ananlysis for the electrohydrodynamic instability of stratified immiscible fluids. *J. Fluid Mech.*, 681:293–310, 2011.

[89] J. Zhang, J. D. Zahn, and H. Lin. A transient solution for deformation under electric fields I: Droplets. *J. Fluid Mech.*, 2012*a*. (submitted).

[90] J. Zhang, J. D. Zahn, and H. Lin. A transient solution for deformation under electric fields II: Vesicles. *J. Fluid Mech.*, 2012*b*. (submitted).

Curriculum Vitae

Jia Zhang

EDUCATION

2007-2012 Ph.D. in Mechanical and Aerospace Engineering, Rutgers University, New Brunswick

2005-2007 M.E. in Fluid Mechanics, Beijing University of Aeronautics and Astronautics, Beijing, China

2001-2005 B.E. in Engineering Mechanics, Beijing University of Aeronautics and Astronautics, Beijing, China

PUBLICATIONS

Zhang, J., Zahn, J. D. and Lin, H. 2012 A transient solution for deformation under electric fields I: Droplets. *J. Fluid Mech.* (submitted).

Zhang, J., Zahn, J. D. and Lin, H. 2012 A transient solution for deformation under electric fields I: Vesicles. *J. Fluid Mech.* (submitted).

Zhang, J., Zahn, J. D. and Lin, H. 2011 A general analysis for the electrohydrodynamic instability of stratified immiscible fluids. *J. Fluid Mech.* **681**, 293-310.

Zhang, J. and Wu S. P. 2008 Numerical simulation of supersonic inlet flow fields based on CFD. *Computer Simulation* **25** (6), 75-78.